All Photonic Isolator using Atomically Thin (2D) Bismuth Telluride (Bi_2Te_3)

Saswata Goswami, Bruno Ipaves, Juan Gomez Quispe, Caique Campos de Oliveira, Surbhi Slathia, Abhijith M.B., Varinder Pal, Christiano J.S. de Matos, Samit K. Ray, Douglas S. Galvao, Pedro A. S. Autreto*, and Chandra Sekhar Tiwary*

Section S1. Synthesis and Characterization of 2D-Bi_2Te_3 nanostructure

Pure Bismuth (99.99%) and Tellurium (99.99%) were combined in a 2:3 molar ratio to produce crystals of Bismuth Telluride (Bi_2Te_3). Bulk Bi_2Te_3 was synthesized by flame-melting the mixture at 850 ± 50 °C for 10 minutes under a sealed argon atmosphere. The material was then cooled using a furnace. The bulk material was subsequently annealed at 450°C under N_2 gas in a sealed quartz tube within a muffle furnace. The bulk crystal was pulverised into powder form with a mortar and pestle. This powder was subsequently probe-sonicated in isopropyl alcohol (IPA) for 4 hours using a Rivotek SM250PS ultrasonic probe sonicator. After a 12-hour rest, the suspended solution was centrifuged at 2000 revolutions per minute for 30 minutes using a REMI PR-24 centrifuge. The 2D Bi_2Te_3 was subsequently extracted from the suspension, making this synthesis technique straightforward and brief.

X-Ray Diffraction: The XRD analysis was performed using the Bruker D8 Advance with Cu-K_α radiation (K_α=1.54 Å). X-ray diffraction (XRD) analysis reveals that identical peaks are seen in both the bulk and 2D structure of the material.[1] **Figure S1a** demonstrates that the structure remains intact during the exfoliation process. The reflections along (006), (015), (222), (1010), (0015), (1016), (0210), (0120) and (1115) exhibit sharp and strong characteristics, with corresponding 2θ values of 17.29°, 27.59°, 37.81°, 44.432°, 53.97°, 57.04°, 62.16° and 65.80° respectively. Figure S1a presents the X-ray diffraction (XRD) pattern for both the bulk and 2D Bi_2Te_3, revealing rhombohedral $R\bar{3}m$ space group with D_{3d}^5 point symmetry crystal structure. All peaks of the XRD pattern matched with the rhombohedral phase of Bi_2Te_3. (ICDD PDF card No. 00-015-0863, a= 4.386 Å, c= 30.497 Å). Rietveld Refinement[2] is performed to refine the lattice parameters, and the results converge to the weighted and expected residual factors R_{wp} = 0.0806 and R_p = 0.0596, yielding a structure in the rhombohedral space group. $R\bar{3}m$ with lattice parameters of a = 4.3963 Å and c = 30.52322 Å. The pseudo-voigt function is chosen to fit the peak profile during the refinement process, which secures a goodness of fit $\chi^2 = (\frac{R_{wp}}{R_{exp}})^2 = 1.82$. A fitted graph is shown in Supporting Information Figure S2. Rietveld refinement is done using the Topas software.

Transmission Electron Microscopy: A high-resolution transmission electron microscope (NEOARM/JEM-ARM200F) was used to image the exfoliated 2D Bi_2Te_3 nanostructure. Figure S1b illustrates the enlarged depiction of the 2D flake-like nanostructure. Figure S1b depicts translucent sheets arranged in a stacked formation, with the grid and the sample clearly discernible. A 3D map is presented in Figure S1c to illustrate the staircase-like layered structure in terms of intensity variation. As depicted in Figure S1d, a cluster of 2D flake-type nanostructures of 2D Bi_2Te_3 is visible. The Top inset of Figure S1d illustrates the Fast Fourier Transform (FFT) SAD pattern corresponding to the (110) rhombohedral plane. The determined value of d spacing for the (110) plane was 0.2074 nm (shown in the bottom inset of Figure S1d). Figure S1d illustrates the enlarged depiction of the 2D flake. The upper inset of Figure S1d presents the selected area electron diffraction (SAED) pattern corresponding to the region marked in red. The lower inset shows the d spacing derived from the IFFT of the SAED pattern.

Atomic Force Microscopy: An atomic force microscope (Agilent Technologies, 5500) was used to evaluate the thickness and lateral width of the two-dimensional Bi_2Te_3 (shown in Figure S1e). Figure S1f illustrates the width profile of the 2D flakes, which ranges from 60 to 140 nm. The average width is 100 nm. Figure S1g shows that the thickness distribution of 2D Bi_2Te_3 spans roughly 0-8 nm, with some particles exhibiting markedly larger thicknesses. The average thickness is 3.5 nm.

Scanning Electron Microscopy: Scanning electron microscopy was performed using a JEOL JSM-IT300HR microscope. Figure S1h shows the SEM image, and Figures S1i and S1j show the EDX mapping image of Bi and Te elements. The schematic indicates that elements are uniformly distributed across the nanostructure. The EDX spectrum shown in the Supporting Information Figure S3 indicates that the Bi / Te atomic ratio of the nanostructure is found to be near 2:3. However, the presence of excess Bi atomic percentage indicates P-type behavior in the nanostructure. Due to the low melting point of Te, some amount of Te might have evaporated during the melting process, which induces P-type behavior in the nanostructure. EDAX spectrum of 2D Bi_2Te_3 is shown in Supporting Information Figure S4.

UV-Vis Spectroscopy: Figure S1n shows that UV-Vis spectroscopy was used to assess the optical absorbance of 2D Bi_2Te_3 in IPA. Figure S1o shows the Tauc plot that was used to estimate the direct bandgap of the 2D Bi_2Te_3. The Tauc plot is described in the following expression,

$$(\alpha h\nu)^{1/n} = A(h\nu - E_g) \quad \ldots\ldots\ldots\ldots\ldots\ldots (1)$$

Here α is the optical absorption coefficient, $h\nu$ is the discrete photon energy, E_g is the bandgap of the material, and n is the order of the polynomial; n is considered as $1/2$, as the material has a direct bandgap nature. The bandgap is calculated to be 0.9 eV.

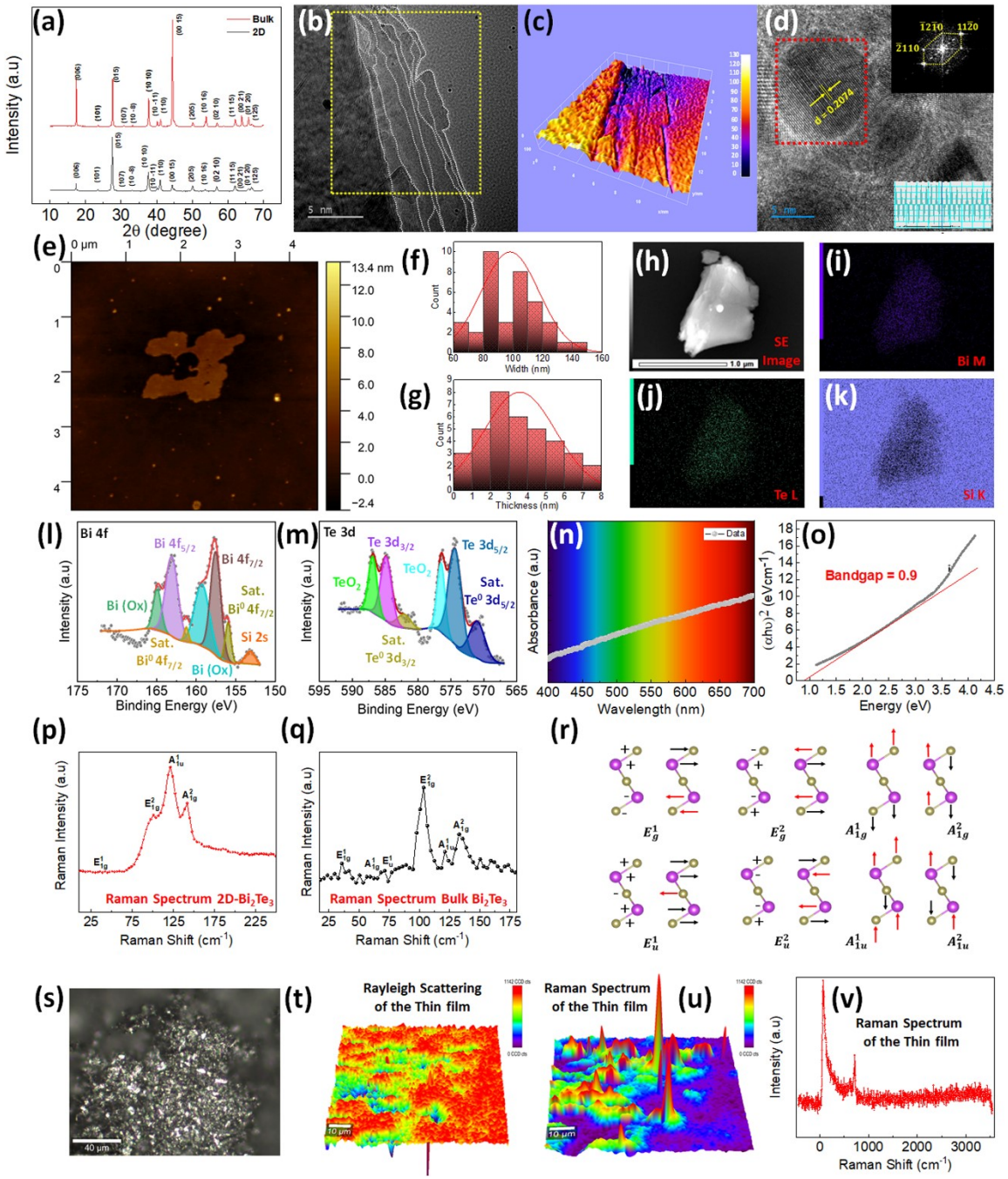

Figure S1. Characterization of 2D Bi_2Te_3. (a) Bulk and 2D Bi_2Te_3 XRD comparison. (b) Transmission electron microscopy image of the 2D Bi_2Te_3 showing two-dimensional morphology. Dotted lines showing one flake on top of another. (c) Figure showing a 3D map of pixel intensity profile done using ImageJ software, showing flakes stacked over each other. (d) Figure showing a single 2D Bi_2Te_3 flake-like nanostructure. Inset showing FFT pattern of (110) plane matched with plane orientation showing (110) plane. Bottom inset showing the calculated d-spacing value. (e) AFM image of the flake-like nanostructure distributed on the surface. Figures (f) and (g) show the width (lateral dimension) and height (thickness) of the exfoliated 2D-Bi_2Te_3. (h) SEM image of the exfoliated nanostructure showing layered morphology. Elemental mapping on the exfoliated nanostructure shows (i) Bi, (j) Te, and (k) Si substrate. The high-definition XPS spectrum of (l) Bi 4f and (m) Te 3d orbitals. Figure (n) showing absorbance spectrum derived from UV-vis Spectroscopy. Figure (o) showing the determined value of the direct

bandgap using the Tauc plot. Figures (p) and (q) show the Raman spectrum of 2D Bi_2Te_3 and the bulk form, respectively. (r) Schematic showing different vibrational modes of 2D Bi_2Te_3. (s) Figure showing a thin film of 2D Bi_2Te_3. Raman mapping taken from the film shown in the previous Figure shows (t) Rayleigh, (u) Raman Signal of the corresponding sample. (v) Raman spectrum of the thin film.

X-Ray Photoelectron Spectroscopy: The IPA solution containing 2D Bi_2Te_3 was then drop-cast on a Si wafer for chemical analysis. PHI 5000 VERSA PROBE III ULVAC PHI (Physical Electronics) was used for the XPS analysis. Supporting Information Figure S4 displays the chemical characterization data obtained by XPS (X-ray photoelectron Spectroscopy, the XPS survey spectrum spans the binding energy range from 0 to 1100 eV.

The peaks observed in the survey spectrum were identified as Te, Bi, C, and O. Figure S1l shows the high-resolution XPS scan of the Bi 4f doublet peaks at about 158.5 and 164 eV, corresponding to the Bi $4f_{7/2}$ and Bi $4f_{5/2}$ energy levels, respectively. The peaks may be separated into two distinct signals located at 157.6 eV and 163.12 eV. These signals are associated with Bi-Te bonds, confirming the formation of the Bi_2Te_3 phase.[3-7] In addition, two peaks at 159.3 eV and 165 eV correspond to those observed in bismuth oxide (BiO_x), indicating the potential development of a surface oxidation phase.[4, 8] The redox signals that reflect the oxidation and reduction potential of Bi oxide species show a relationship with the oxidation of Bi^0 films and the reduction of Bi^{3+} ions. The double peaks at 156 eV and 165 eV correspond to the Bi^0 peak, or elemental bismuth present in the sample, which may be due to surface-exposed Bi atoms. In addition, Figure S1m displays the Te 3d peaks, which consist of two doublets that can be separated into three component peaks each. The peaks at 573.8 eV and 584.1 eV are characteristic peaks of the 2D Bi_2Te_3 semiconductor phase. [9-11] Similarly, we observe two peaks at 574 eV and 586.87 eV, which are associated with the Te^{4+} state and may be due to the presence of the TeO_2 phase. The peaks at 577.2 and 587.6 eV correspond to the Te^0, which is also probably a feature of the exposed Te atom surface. [5, 12, 13] The Te^{2+} atoms are predominantly located on the surface of the material. The TeO_2 peaks arise from the reaction between Te^{4+} atoms distributed on the surface of the sample and oxygen present in the surrounding air.[13] Supporting Information Figure S5a indicates the presence of C in the sample. Deconvolution of the peaks reveals two distinct subpeaks corresponding to C-O-C and C-C.[14,15] Both peaks are located at 283.62 eV and 285.62 eV, respectively. The presence of C peaks is most likely attributed to the sample preparation conditions.[16] In contrast, the oxygen peaks confirm the inherent inclination of the Te^{4+} state to interact with the surrounding air, hence causing surface oxidation. This is supported by the double peaks seen for Bi and Te in Figure S5b.[17]

In particular, the O 1s spectrum shown in Supporting Information Figure S5b displays three distinct bonding types at 528.87 eV, 531.25 eV, and 532 eV. The dominant signal at 531.25 eV in the Bi-Te

samples may be linked to lattice oxygen resulting from metal-oxide interactions.[4] In conclusion, the small intensity peaks seen at 532 eV and 528.87 eV are associated with the presence of dangling bonds O^- and O^{2-}, as well as surface adsorbed oxygen O^{2-}, respectively. The peak at 532 eV may indicate the presence of a long-chain organic compound in the sample. This may have happened due to the laboratory conditions.

Raman Spectroscopy: Raman spectroscopy measurement is performed using the WiTec alpha 300 system equipped with a 600 lines/nm grating. The excitation was performed using a 532 nm diode laser with a spot size of 500 nm. The data analysis is carried out using the WiTec project software.

Raman Spectroscopy was used to determine the vibrational modes, and investigating the chemical bonds would provide a wealth of information about the structure and stability of these compounds. According to the TEM and XRD results, few-QL Bi_2Te_3 has a hexagonal nanostructure. Based on group theory, this unit cell belongs to the space group D_3^{d3} $p\bar{3}$m1. In a unit cell each layer consists of five monoatomic planes of $Te^{(1)}$–Bi–$Te^{(2)}$–Bi–$Te^{(1)}$[18, 19], this five atoms arranged in vertical axis occupy ~1nm is measured to be 1 QL. At the Brillouin zone centre (q=0), five atoms produce four Raman-active modes: the in-plane vibrational modes E_g^1 and E_g^2, and the out-of-plane vibrational modes A_{1g}^1 and A_{1g}^2. Group theory classification indicates that there are 12 optical modes represented as $2A_{1g} + 2E_g + 2A_{1u} + 2E_u$.[20] The phonon modes in this material are considered to be Raman or infrared (IR) active because of the crystal's inversion symmetry. The A_{1g} and E_g modes demonstrate 2-fold degeneracy.

The atoms oscillate within the same plane and perpendicular to it in diverse phonon modes. In E_g modes, the atoms oscillate inside the basal plane, but in A_{1g} modes, the atoms oscillate along the CH direction. Crystals have inversion symmetry, indicating that the IR-active modes (A_{1u}) must demonstrate odd parity, whereas the Raman-active modes (E_g, A_{1g}) must exhibit even parity under inversion.

A_{1g}^1 mode is the vibration mode that moves towards higher frequencies in the out-of-plane direction. This change relates to alterations in the interlayer van der Waals force along the (0 0 1) direction, induced by dislocations resulting from lattice mismatch and residual internal stress. The Fröhlich electron-phonon interaction stimulates the longitudinal optical, A_{1g}^1 vibration, indicating that the blueshift of the A_{1g}^1 Mode signifies an increase in internal stress due to electron-phonon coupling.[21] According to group theory, the ~121 cm^{-1} peak is attributed to the longitudinal optical phonon mode.[21, 22] The same can be observed in Figure S1p.

Figure S1p illustrates that the Raman intensity of A_{1u}^1 out-of-plane vibrations along the c axis surpasses that of the a-b in-plane lattice vibrations E_{1g}^2, suggesting that the 2D Bi_2Te_3 consists of multiple QLs in thickness.[23-25] The Raman spectra of the thin bulk exhibit a notable result, characterized by an additional

peak of lower intensity at approximately 121 cm^{-1}, as illustrated in Figure S1q. Bi_2Te_3 exhibits a high degree of symmetry and crystalline order in its 2D nanostructure, formed from stoichiometric atoms. The crystal structure significantly influences the IR-active Raman A_{1u}^1 mode. The peak is identified as the A_{1u}^1 mode, comprising longitudinal optical (LO) phonons situated near the boundary of the Brillouin Zone (BZ), particularly at the Z point. The A_{1u}^1 mode is identified as an infrared active mode; however, it has been observed that there is no Raman active mode present in the bulk Bi_2Te_3 crystal.[26] Thus, we may rationally attribute the formation of the IR active A_{1u}^1 mode in thin nanostructures to the violation of crystal symmetry resulting from the occurrence of two surfaces.

This mode has odd parity and is not allowed in bulk crystals due to their inversion symmetry.[27] The presence of the strongest A_{1u}^1 peak can be attributed to the disruption of crystal symmetry on nanoplates with extremely thin thickness. Therefore, the Raman spectra suggest that the thickness of the nanostructure in its original state is not uniform. As seen in Figure S1p, the signal of A_{1u}^1 It is not prominent, indicating that it shows the Raman signature of 2D Bi_2Te_3. However, the A_{1u}^1 is an infrared active mode (IR), the influence of temperature enhances the oscillation of bonded atoms and the collision between electrons and phonons. The temperature effect amplifies the oscillation of bonded atoms and the interaction between electrons and phonons. Figure S1r illustrates the Raman vibrational modes of the 2D Bi_2Te_3. The image in Figure S1 shows the thin film used for Raman mapping. Raman mapping derived from the film depicted in the preceding picture illustrates t) Rayleigh, u) Raman Signal of the corresponding sample. Figure S1v shows the Raman spectrum of the thin film.

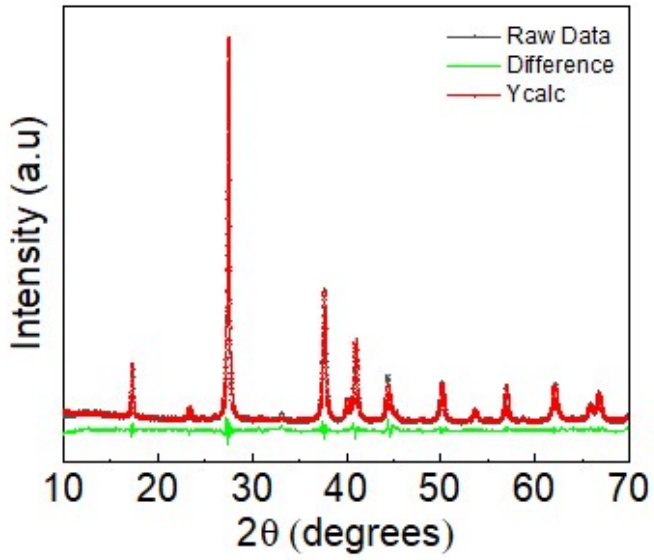

Figure S2: Fitted XRD pattern obtained through Topas software.

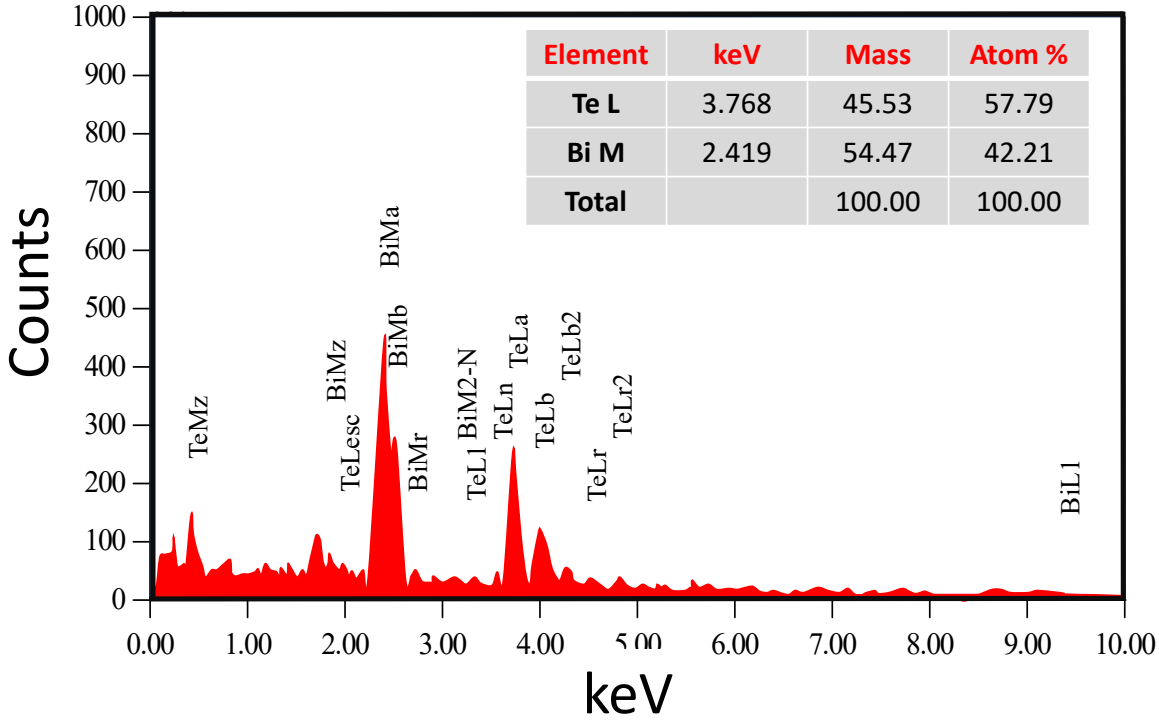

Figure S3: EDX Spectrum of 2D-Bi_2Te_3 nanostructure.

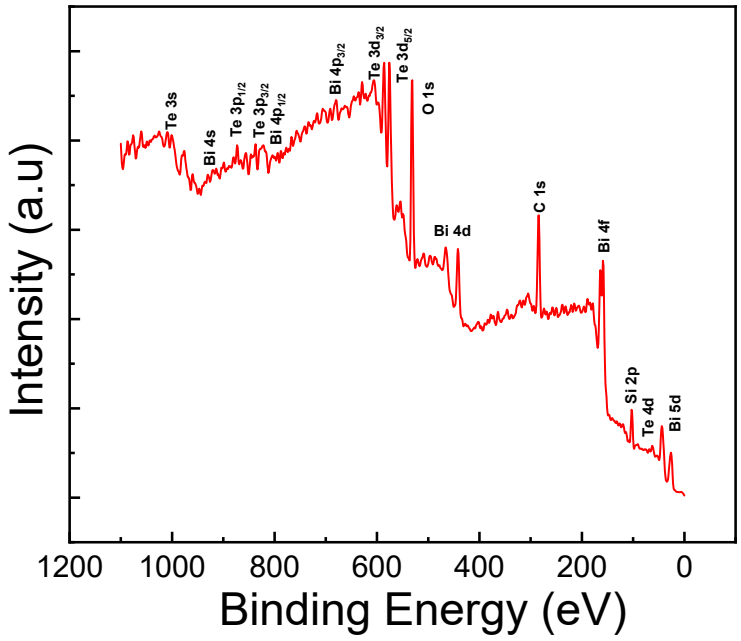

Figure S4: The XPS survey spectrum covering the binding energy range of 0 to 1100 eV.

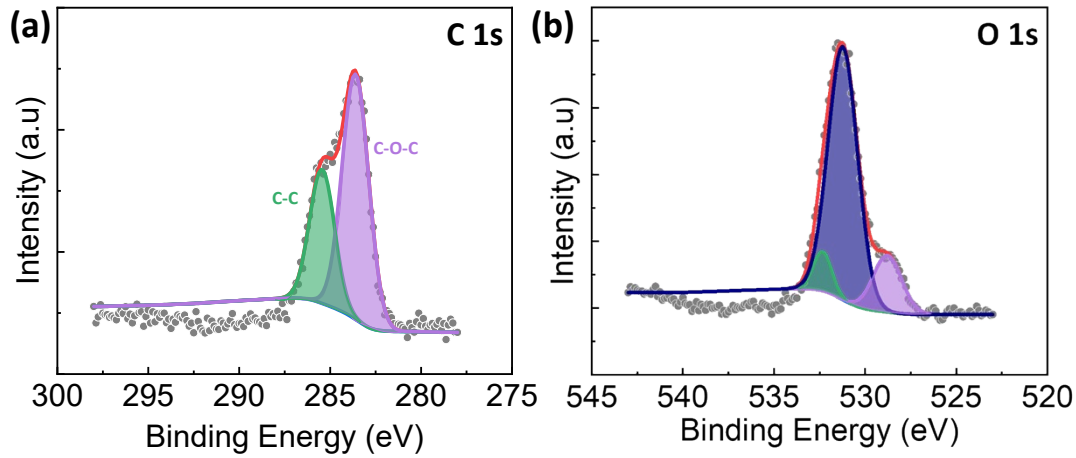

Figure S5: (a) XPS Spectrum of the C 1S. (b) XPS Spectrum of the O 1S.

Section S2: Theoretical Estimation of the Formula of n_2 and $\chi^{(3)}_{total}$

In this work, we investigate the nonlinear Kerr effect, which plays a crucial role in determining the nonlinear optical responses of 2D-Bi_2Te_3. Equation 2 defines the Kerr nonlinear effect by relating the incident laser beam intensity (I) to the refractive index (n).

$$n = n_0 + n_2 I \quad \ldots\ldots\ldots\ldots\ldots\ldots (2)$$

The terms "n_0" and "n_2" represent the linear and nonlinear refractive indices of the material, respectively. [28]

Moreover, a modification in the refractive index of the medium will cause the light wave to undergo a mandatory phase shift. As a result, the light wave transmitted through the medium experiences its own intensity modulation, known as self-phase modulation (SPM). In general, the SSPM phenomenon is excited by a fundamental-mode Gaussian beam (TEM_{00}). A Gaussian beam traverses a nonlinear medium of length L along the z-axis, and its electric field distribution may be characterized as follows:

$$E(r,z) = E(0,z)\frac{\omega_0}{\omega(z)}\exp\left(-\frac{r^2}{\omega(z)^2}\right)\times exp(-i[kz - arctan\frac{z}{z_0} + \frac{kn_0r^2}{2R(z)}]) \quad \ldots\ldots\ldots\ldots\ldots\ldots (3)$$

Where λ is the wavelength of the laser, $k = \frac{2\pi}{\lambda}$ is the wave vector, $z_0 = {\pi\omega_0^2}/{\lambda}$ is the Rayleigh length (the length of the beam that propagates like wave), $R(z) = z\,[1 + (\frac{z}{z_0})^2]$ is the radius of curvature of the wavefront, ω_0 is the beam waist radius at z. Using the radius of the laser beam waist as the starting point for beam propagation, the electric that is incident on the 2D material can be defined as,

$$E(r,z_0) = E(0,z_0)\exp\left(-\frac{r^2}{\omega(z_0)^2}\right) \times exp(-i\frac{kn_0r^2}{2R(z)}) \quad \text{..... (4)}$$

The light intensity distribution can be expressed as,

$$I(r,z) = I_0(1 + z^2/z_0^2)^{-1} exp(-{2r^2}/{\omega_0^2}) \quad \text{..... (5)}$$

Where $I_0 = 2P_{ave}/[\pi\,\omega(z)^2]$ is the central intensity of the Gaussian Beam, P_{ave} is the average power of the laser. Therefore, the refractive index can be expressed as,

$$n(r) = n_0 + n_2 I(r) \quad \text{..... (6)}$$

Assuming a thin sample, the output can be expressed as,

$\Delta\phi = \Delta\psi_L(r) + \Delta\psi_{NL}(r)$, where, $\Delta\psi_L(r) = kn_0r^2/[2R(z)]$ is the linear phase shift, and $\Delta\psi_{NL}(r)$ is a nonlinear phase shift related to the light intensity is described as,

$$\Delta\psi_{NL}(r) = \frac{2\pi n_0}{\lambda}\int_0^L n_2 I(r,z)dz \quad \text{..... (7)}$$

The above-mentioned nonlinear phase shift, "$\Delta\psi$", as shown in Equation 7, is induced by a potent Kerr Nonlinear Effect caused by the incoming Gaussian laser beam,

The transverse propagation wave vector is thus expressed as,

$$\delta k(r) = \frac{d\Delta\psi_{NL}}{dr} = \frac{-8krn_2 I(r,z)exp(-2r^2/\omega_0^2)}{n_0} \quad \text{..... (8)}$$

The character λ denotes the wavelength of the laser, while L_{eff} refers to the effective transmission length of the laser as it travels through the cuvette, $r \in [0, +\infty)$ is the radial coordinate and $I(r,z)$ is the radial intensity distribution [29]

In the outgoing Gaussian light, there are at least two distinct locations, r_1 and r_2, where the slopes of the distribution curve, represented by $(d\Delta\psi/dr)_{r=r_1}$ and $(d\Delta\psi/dr)_{r=r_2}$, are equal and have the same phase. This is evident from the Gaussian distribution of the nonlinear phase shift, as seen in Figure 2b. Thus, the output light intensity profile exhibits a consistent phase difference while maintaining the same slope points. Clearly, these two points meet the requirement for interference. When $\Delta\psi_0 \geq 2\pi$, the diffraction ring appears. The self-induced diffraction pattern is observed as rings, which can be either bright or dark, in the far field. The positioning of these rings is determined by Equation 9.

$$\Delta\psi_{r_1} - \Delta\psi_{r_2} = 2M\pi \quad \ldots\ldots\ldots\ldots\ldots\ldots (9)$$

In this context, M represents an integer. The terms "dark field " and "bright field" correspond to the odd and even values of M, respectively.[30] The phase shift, which is crucial for the SSPM effect, generates a self-diffraction pattern in the far field, as seen in Figure 2(b). The calculation of the effective transmission length (L_{eff}) using Equation 10 is essential for finding the nonlinear refractive index (n_2) as described in Equation 14.[31]

$$L_{eff} = \int_{L_1}^{L_2} \left(1 + \frac{z^2}{z_0^2}\right)^{-1} dz = z_0 arctan\left(\frac{z}{z_0}\right)\Big|_{L_1}^{L_2},\ z_0 = \frac{\pi\omega_0^2}{\lambda} \quad \ldots\ldots\ldots\ldots\ldots\ldots (10)$$

L_2 and L_1 denote the distance between the laser beam's focus and the quartz cuvette's boundaries in this particular situation. The thickness of the quartz cuvette is calculated to be $L_2 - L_1$. The intensity profile of the transmitted beam follows a Gaussian distribution, with the highest intensity at the center, $I(0,z) = 2I$. Here I represent the mean intensity of the incoming laser beam z_0 is the diffraction length and ω_0 denotes the beam radius ($\frac{1}{e^2}$).

The Light Intensity is included in the expression of $\Delta\psi_{NL}(r)$,

$$\Delta\psi(r) = \frac{2\pi n_0 n_2}{\lambda} I_o L_{eff} e^{-2r^2/\omega_0^2} \quad \text{..... (11)}$$

Also, $\Delta\psi(r_1) - \Delta\psi(r_2) = M\pi$, the brightness of the diffraction ring is decided upon the phases of radial distances on two beams (r_1) and (r_2). The center and infinity position of the gaussian beam is satisfied as,

$$\Delta\psi(0) - \Delta\psi(\infty) = 2N\pi \quad \text{..... (12)}$$

Where N is the number of diffraction rings, and

$$\Delta\psi(\infty) = 0, \Delta\psi(0) = \frac{2\pi n_0 n_2}{\lambda} I_0 L_{eff} \quad \text{..... (13)}$$

The nonlinear refractive index n_2 is expressed as,

$$n_2 = \left(\frac{\lambda}{2n_0 L_{eff}}\right).\frac{dN}{dI} \quad \text{..... (14)}$$

The dN/dI is an important parameter to evaluate the nonlinear refractive index of the two-dimensional material. The third-order nonlinear susceptibility $\chi^{(3)}_{total}$ is employed to characterize the nonlinear optical characteristics of materials.[32-34]

It can be written as

$$\chi^{(3)}_{total} = \frac{cn_0^2}{12\pi^2} 10^{-7} n_2 \ (e.s.u) \quad \text{..... (15)}$$

Here, c represents the speed of light in free space, n_0 is the linear refractive index of the IPA solvent, and n_2 defines the effective length that the laser beam propagates through the cuvette. However, the effective number of 2D materials available in the cuvette has a direct effect on the value of the $\chi^{(3)}_{total}$. Hence, it is necessary to determine the value of third-order nonlinear susceptibility caused by a single layer of two-dimensional sheets, $\chi^{(3)}_{monolayer}$. The relationship between the overall electric field strength E_{total} and the electric field strength $E_{monolayer}$ traveling through the single layer of Bi_2Te_3 may be mathematically represented as,[30, 35]

$$E_{total} = \sum_{j=1}^{N_{eff}} E_j \cong N_{Eff}\, E_{monolayer} \quad \text{..... (16)}$$

In this context, N_{Eff} represents the number of 2D-Bi_2Te_3 layers present in the solution, through which the beam passes. The relationship between $\chi^{(3)}_{total}$ and $\chi^{(3)}_{monolayer}$ can be expressed as, [34-36]

$$\chi^{(3)}_{total} = N^{2}_{eff}\chi^{(3)}_{monolayer} \quad \text{..... (17)}$$

Section S3: Calculation of the effective number of 2D-Bi_2Te_3 nanostructures present in the solution

The molecular weight of Bi_2Te_3 is 800.7608 g · mol^{-1}. The concentration can be expressed as 3.122×10^{-4} mol. L^{-1}. The cuvette volume is considered to be 4.5×10^{-3} L. The Total number of molecules of Bi_2Te_3 in the solution is $M = \rho \times V \times N_A$ (N_A is Avogadro's constant). The space group of the Bi_2Te_3 is $R\bar{3}m$, which is a hexagonal crystal system, and lattice constants are found to be a = 4.386 Å and c = 30.49 Å, respectively. Thus, a single effective layer contains a number of molecules $m = 1 \times 4.5\ cm^2 / (Sin\ 90°) \times (4.386)^2 = 2.079 \times 10^{15}$ molecules. The number of layers of the nanoflakes can be calculated as follows: $n = M/m = 361$.

Table S1. The value of n_2 and $\chi^{(3)}_{total}$ calculated using SSPM Spectroscopy in recent literature.

2D Material	Type of laser	n_2	$\chi^{(3)}_{total}$	$\chi^{(3)}_{monolayer}$	References
Graphene	CW 532 nm	2.5×10^{-9} m^2.W^{-1}	1×10^{-3}	1×10^{-7} (e.s.u.)	30
MoS_2	CW 478 nm	10^{-7}	1.44×10^{-4}	1.6×10^{-9} (e.s.u.)	32
$Ti_3C_2Ti_x$	CW 457 nm/ 532nm / 671 nm	11×10^{-4} / 4.75×10^{-4}/ 4.72×10^{-4}	-----	4.34×10^{-7}/ 1.68×10^{-7}/ 0.15×10^{-7} (e.s.u.)	37
2D Te NS	CW 457 nm/ 532nm / 671 nm	6.14×10^{-5}/ 6.202×10^{-5}/ 7.37×10^{-5}	------	-------	38
Sb FS/QD	CW 532 nm / 633 nm	FS - 2.88×10^{-5} / 0.979×10^{-5} QD- 1.91×10^{-5}/ 0.719×10^{-5}	FS - 3.98×10^{-9} / 1.74×10^{-9} QD- 2.87×10^{-5}/ 1.29×10^{-5}	-----	39
Bi_2Te_3	CW 1070 nm	2.91×10^{-9} m^2.W^{-1}	10^{-3}	10^{-8} (e.s.u.)	40
Graphene Oxide	CW 532 nm CW 671 nm	3.57×10^{-6} cm^{2}W^{-1} 1.1×10^{-6} cm^{2}W^{-1}	1.7×10^{-6} 5.32×10^{-6}	------	41
$MoTe_2$	CW 473 nm /532 nm/ 750 nm/ 801 nm	------	-------	1.88×10^{-9} (e.s.u.) 1.3×10^{-9} (e.s.u.) 1.14×10^{-9} (e.s.u.) 0.98×10^{-9} (e.s.u.)	42
$NbSe_2$	532 nm / 671 nm /	1.352×10^{-5} m^2.W^{-1} / 2.0×10^{-5} m^2.W^{-1}/ 1.07×10^{-5} m^2.W^{-1}	1.352×10^{-5} / 9.354×10^{-6} / 5.03×10^{-6}	3.34×10^{-9}/2.59×10^{-9} /3.39×10^{-9} (e.s.u.)	43
Bi_2Se_3	350 nm/ 600nm/ 700nm/ 1160 nm	1.16×10^{-8} / 3.53×10^{-9} / 2.5×10^{-9}/ 1.65×10^{-9} (m^2.W^{-1})	5.76×10^{-3} /1.82×10^{-3} / 1.29×10^{-3} /8.53×10^{-4} (e.s.u.)	10^{-8}/ 10^{-8} / 10^{-9}/ 10^{-9} (e.s.u.)	44
Black Phosphorus	Pulsed Laser 350-1160 nm	10^{-5} cm^2.W^{-1}	10^{-8} (e.s.u.)	-----	31
WSe_2	CW 532nm / 671 nm/ 457 nm/	2.94×10^{-6} / 8.66×10^{-6} / 6.402×10^{-6}	1.371×10^{-6}/ 4.04×10^{-6}/ 2.98×10^{-6}	8.14×10^{-10}/ 8.44×10^{-11} /3.69×10^{-9} (e.s.u.)	29
TaS_2	CW 532nm / 671 nm/ 457 nm	1.14×10^{-5}, 0.88×10^{-5}, 0.69×10^{-5} cm^{2}W^{-1}	------	1.2×10^{-6}/ 0.9×10^{-6}/ 0.7×10^{-6} (e.s.u.)	45
$TaSe_2$	532 nm / 671 nm	8.0×10^{-7}/ 3.3×10^{-7} (cm^2.W^{-1})	1.37 x 10^{-7} /1.58 X 10^{-7}	3.1×10^{-10}/1.64×10^{-10} (e.s.u.)	34
GeSe	532 nm	4.841×10^{-6} (cm^2.W^{-1})	2.258×10^{-6}	2.945×10^{-10} (e.s.u.)	46
Boron NS	CW 457 nm / 532nm /671 nm	1.25×10^{-5} / 3.43×10^{-6} / 9.45×10^{-6} (cm^2.W^{-1})	1.75×10^{-7} / 0.64 X 10^{-6}/ 0.48 X 10^{-6} (e.s.u.)	4×10^{-9}/ 1.8×10^{-9}/ 1.8×10^{-9} (e.s.u.)	47
SnS NS	CW 532 nm/ 633 nm	4.531×10^{-5}/ 0.323×10^{-5} (cm^2.W^{-1})	2.317×10^{-5}/0.165×10^{-5} (e.s.u.)	6.995×10^{-10} / 2.037×10^{-10} (e.s.u.)	48
Bi_2S_3	CW 457nm/ 532 nm/ 671 nm	3.34×10^{-5}/ 1.26×10^{-6}/ 1.62×10^{-7}(cm^2.W^{-1})	------	-------	49
$MoSe_2$	CW 532nm	3.24 × 10-10 W.m^{-2}	--------	1.1×10^{-9} (e.s.u.)	50
TaAs	405 nm/ 532 nm/ 671 nm/ 841 nm	-------	6.06×10^{-4} / 5.68×10^{-4} / 5.30×10^{-4}/ 4.65×10^{-4} (e.s.u.)	10.50×10^{-9} / 9.86×10^{-9} /9.19×10^{-9} / 8.07×10^{-9} (e.s.u.)	51
$NiTe_2$	CW 650 nm/ 532 nm / 405 nm	3.22×10^{-5}/ 6.15×10^{-5} / 7.68×10^{-5} (W.cm^{-2})	1.56×10^{-3} / 2.99×10^{-3} / 3.76×10^{-3}	4.06×10^{-9}/ 7.79×10^{-9}/ 9.89×10^{-9} (e.s.u.)	52
Violet Phosphorus NS	CW 405 nm/ 473 nm / 532 nm/ 671 nm/ 721 nm	--	--	3.54×10^{-8}/ 1.65×10^{-8}/ 9.64×10^{-9}/ 4.63×10^{-9}/ 2.31×10^{-9} (e.s.u.)	53

Hybrid Bismuth Halide $(PPA)_3BiI_6$	CW 405 nm/ 473 nm / 532 nm	--	--	1.77×10^{-8}/ 1.26×10^{-8}/ 7.74×10^{-8} (e.s.u.)	54
MoP Microparticles	CW 532 nm	1.91×10^{-5} (W/cm^2)	--	--	55
$Fe_{3-x}GeTe_2$, $Fe_{4-x}GeTe_2$, $Fe_{5-x}GeTe_2$	671 nm / 532 nm	2.49×10^{-5} (W.cm^{-2})/ 2.16×10^{-5} (W.cm^{-2}), 1.23×10^{-5} (W.cm^{-2})/ 1.09×10^{-5} (W.cm^{-2}), 0.93×10^{-5} (W.cm^{-2})/ 0.92×10^{-5} (W.cm^{-2})	--	2.75×10^{-8}/ 2.37×10^{-8}, 1.57×10^{-8} /1.39×10^{-8},1.3×10^{-8} /1.29×10^{-8} (e.s.u.)	56
Bi_2Te_3 (Our work)	CW 650 nm/ 532 nm / 405 nm	2.7×10^{-4}/ 8.14×10^{-5} / 10.1×10^{-5} (W.cm^{-2})	1.56×10^{-3} / 4.741×10^{-3} / 5.88×10^{-3}	1.2×10^{-7}/ 3.63×10^{-7} / 4.51×10^{-9} (e.s.u.)	

Table S2. SSPM formation time of the diffraction pattern as reported in the relevant literature.

Material	Laser Specification	Solvent	Intensity	Formation time (T)	Ref.
$MoTe_2$	473/ 532/ 750 nm (CW)	NMP	252 W.cm^{-2}	0.45 s/ 0.6 s/ 0.62 s	42
$MoSe_2$	671 nm (CW)	NMP/ Acetone	12 W.cm^{-2}	0.41 s/ 0.22 s	43
TaAs	589 nm/ 532 nm/ 473 nm (CW)	NMP	90 W.cm^{-2}	2.5 s/ 2.5 s/ 2.3 s	51
Graphene Oxide	532 nm (CW)	IPA	----	0.43 s	57
Black Phosphorus	700 nm (CW)	NMP	18.9 W.cm^{-2}	0.7 s	31
Violet Phosphorus	CW 405 nm/ 473 nm / 532 nm/ 671 nm/ 721 nm	NMP	1.55 W.cm^{-2} / 3.55 W.cm^{-2} / 9.80 W.cm^{-2} / 19.65 W.cm^{-2} / 18.64 W.cm^{-2}	0.3 s/ 0.47 s/ 0.7s/ 0.83 s/ 0.77 s	58
MoP Microparticles	CW 532 nm	NMP	219.8 W.cm^{-2}	0.4 s	55
$Fe_{3-x}GeTe_2$, $Fe_{4-x}GeTe_2$, $Fe_{5-x}GeTe_2$	671 nm / 532 nm	NMP	15 W.cm^{-2}	0.28/ 0.31, 0.16/ 0.23, 0.15/0.18	56
Bi_2Te_3	650 nm/ 532 nm/ 405 nm	NMP	10.318 W.cm^{-2}, 5.39 W.cm^{-2}, and 1.244 W.cm^{-2}	0.266 s, 0.5 s ,0.3999 s	

Section S4: Computational Details

We investigated the interaction between the molecules isopropyl alcohol (IPA)[59] and N-methyl-2-pyrrolidone (NMP)[60] with the host material 2D-Bi_2Te_3[61] using density functional theory (DFT)[62]. The calculations were conducted with the SIESTA software[63, 64], employing a plane-wave basis set with an energy cutoff of 350 eV. In SIESTA, the Kohn-Sham orbitals were expanded using a double-zeta basis set of numerical pseudoatomic orbitals of finite range, augmented with polarization orbitals. We used optimized pseudopotentials and atomic bases from the SIMUNE database[65] with the Perdew-Burke-Ernzerhof (PBE) approximation for the exchange-correlation functional[66]. The Dion et al. scheme[67], optimized by Klimes et al. (optB88-vdW)[68], was employed to accurately describe dispersive van der Waals (vdW) interactions. Bader charge analysis was conducted to quantify the charge transfer between the IPA and NMP molecules and the host material, 2D-Bi_2Te_3.[69]

The total energy convergence threshold for electronic calculation was 1×10^{-4} eV. Geometry optimizations were carried out using the conjugate gradient (CG) algorithm, ensuring that the magnitude of the forces acting on each ion was minimized to less than 0.01 eV/Å for the primitive cell of 2D-Bi_2Te_3 and less than 0.02 eV/Å for a 4×4×1 supercell. The irreducible Brillouin zone was sampled with a 5×5×1 k-point mesh for the primitive cell and a 2×2×1 k-point mesh for the 4×4×1 supercell[70].

Before constructing the heterostructure composed of IPA or NMP and 2D-Bi_2Te_3, we optimized the primitive cell of 2D-Bi_2Te_3 using SIESTA. The unit cell dimensions for the 2D-Bi_2Te_3 were found to be a=b=4.40 Å, which are in good agreement with the literature[61], while the lattice parameter perpendicular to the sheets (z-axis) was fixed at c= 30 Å. Subsequently, a 4×4×1 supercell of 2D-Bi_2Te_3 was optimized with lattice parameters a = b= 17.62 Å and c = 30 Å. To construct the 2D-Bi_2Te_3 and molecule heterostructure, we minimized the total energy with respect to the distance between the molecules and the surface in the z-direction. Initially, the molecules were placed approximately 1.5 Å from the 2D-Bi_2Te_3 surface, and the distance was incrementally increased by 0.5 Å. After determining the most favorable distance, we optimized the systems by allowing only the molecules to move.

We have also calculated the binding energy (Eb) using the following Equation[71, 72]:

$$E_b = E_{Bi_2Te_{3+Mol}} - (E_{Bi_2Te_3} + E_{Mol}) \quad \text{..... (18)}$$

In this expression, $E_{Bi_2Te_{3+Mol}}$ represents the total energy of the system with the molecule (IPA or NMP) adsorbed onto the 2D-Bi_2Te_3 surface, $E_{Bi_2Te_3}$ is the total energy of the pristine 2D-Bi_2Te_3, and E_{Mol} denotes the energy of the isolated molecule (IPA or NMP).

To investigate charge redistribution during adsorption, we performed a charge density difference analysis (CDD). This involved calculating the charge density of the pristine 2D-Bi_2Te_3 surface, the charge density

of the surface with the adsorbed molecule ($^{\rho_{Bi_2Te_3+Mol}}$), and the charge density of the isolated molecule (IPA or NMP), using the following Equation[72-74]:

$$\Delta\rho = \rho_{Bi_2Te_3+Mol} - (\rho_{Bi_2Te_3} + \rho_{Mol}) \quad \text{..... (19)}$$

Regions where $\Delta\rho > 0$ indicate charge accumulation, while the ones where $\Delta\rho < 0$ indicate charge depletion.

Section S5. Intensity Dependent Dynamic Collapse of Diffraction Pattern and Variation in Nonlinear Refractive Index with Different Solvents

Through further examination of the SSPM phenomenon, it becomes clear that the self-diffraction pattern displays a phenomenon of distortion as time progresses. At some point, when the diffraction pattern exhibits the maximum vertical diameter, the upper portion of the pattern begins to converge towards the middle region of the diffraction pattern. Vertical distortion is more prominent than horizontal distortion as seen in **Figure S6a**. Initially documented by Wang et al.[75] this distortion of the pattern can be described by non-axis thermal convection, which elucidates the underlying mechanism of the collapse process. The values R_H and θ_H are designated as the maximum radius and the associated half-cone angle, respectively, before the collapse process [48, 76]. The relationship can be represented as,

$$\theta_H = \frac{R_H}{D} \quad \text{..... (20)}$$

Equation 20 is valid only if D >> R_H. The parameter D defines the distance from the cuvette to the screen. Over time, thermal convection distorts the diffraction pattern, altering both the maximum diffraction radius R_h and the half-cone angle θ_h. If $D >> R_{h,}$ therefore, the relationship may be represented as,

$$\theta_h = \frac{R_h}{D} \quad \text{..... (21)}$$

Hence, the measurement of distortion is expressed in terms of the distortion radius (R_D) and the distortion angle (θ_D). The relationship might be characterized as,

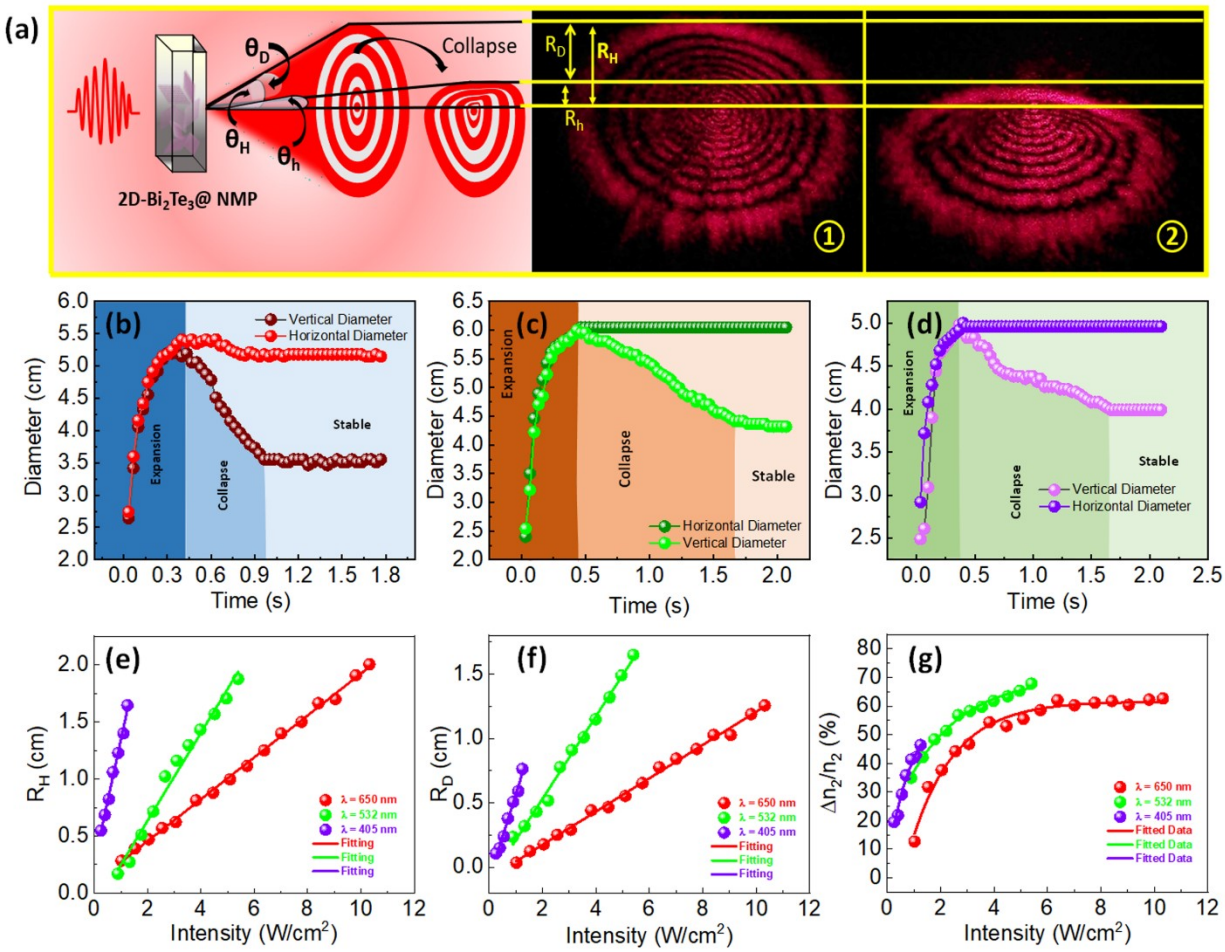

Figure S6. Figurative depiction of the dynamic collapse process. (a) Graphical depiction of the collapse phenomenon of the SSPM diffraction pattern featuring a semi-cone and distortion angle for 2D Bi_2Te_3 in NMP solvent. (b-c-d) The temporal evolution of the vertical and horizontal diameters over various wavelengths (λ = 650, 532, and 405 nm) in NMP solvent. (e) The variation in maximum radius (R_H) with intensity across different wavelengths (λ = 650, 532, and 405 nm) in NMP solvent. (f) The change in the distorted radius (R_D) with changing intensity for different wavelengths (λ = 650, 532, and 405 nm) in NMP solvent. (g) The analysis of the variation of n_2 (nonlinear refractive index) with varying intensity across different wavelengths (λ = 650, 532, and 405 nm) in NMP solvent.

$$\theta_H - \theta_h = \frac{R_D}{D} \quad \ldots\ldots\ldots\ldots\ldots\ldots\ldots (22)$$

Furthermore, the half-cone angle may be approximated as,

$$\theta_H = \frac{\lambda}{2\pi}\left(\frac{d\psi}{dr}\right)_{max}, r \in [0, +\infty] \quad \ldots\ldots\ldots\ldots\ldots\ldots (23)$$

Here, r represents the transverse position of the beam. For a Gaussian beam, the above Equation can be θ_H can also be expressed as,[77]

$$\theta_H = n_2 IC \quad \text{..... (24)}$$

Where $C = [\ -\frac{8rL_{eff}}{\omega_0^2}\exp\left(-\frac{2r^2}{\omega_0^2}\right)\ ]$ is constant when $r \in [0, +\infty)$. Figure S6a illustrates the evolution of the diffraction pattern for the wavelength 650 nm. The variance in distortion may be quantified by analyzing the angle of distortion between the sample and the screen, with the degree of distortion dependent on the intensity.[36] Consequently, we may determine the collapse angle as follows,

$$\theta_D = \theta_H - \theta_h = \left(n_2 - n_2^{'}\right)IC = \Delta n_2 IC \quad \text{..... (25)}$$

The distortion observed in the top region of the diffraction pattern is due to the non-uniform fluid motion induced by heat, which lacks symmetry along the axis, leading to the collapse of the diffraction pattern.[75] The thermal convection occurs as a result of the laser beam's propagation, causing the solvent to heat up due to its absorption coefficient being constant [36, 78]. Due to the indirect effect of laser heating, a temperature gradient is created at a right angle to the axis of the laser point, which enhances the process of 'thermal convection'. Based on the information provided in Equations 24 and 25, it can be inferred that,

$$\frac{\Delta n_2}{n_2} = \frac{\theta_D}{\theta_H} = \frac{R_D}{R_H} \quad \text{..... (26)}$$

Using Equation 26, we may determine the relative change of the nonlinear refractive index by observing the dynamic change($\frac{\theta_D}{\theta_H}$) or ($\frac{R_D}{R_H}$) in the distortion of the diffraction ring. The value of $\Delta n_2/n_2$ is influenced by various factors such as laser wavelength, temperature, and duration.[79] Although the value of $\Delta n_2/n_2$ is primarily dependent on the incoming laser intensity.[46,77] The value of $\Delta n_2/n_2$ can be determined using mathematical computation.

Figure S6a(①-②) displays the image captured by the CCD camera. The diffraction pattern exhibits the maximum number of rings and the greatest vertical diameter, and the condition of equilibrium is observed following the collapse phenomenon, when the laser beam has a wavelength of 650 nm. Figure S6b–d illustrates the temporal development of the diffraction ring pattern with progression of time for three laser beams with wavelengths (λ) values of 650, 532, and 405 nm, respectively, at their maximum laser intensity. All three lasers exhibited a progressive increase in horizontal diameter over time, reaching a maximum, after which they remained constant. Simultaneously, the vertical diameters attain their maximum magnitude and then gradually diminish over time to reach a constant value. After reaching a certain ring number, the thermal convection process becomes prominent, and distortion in the diffraction pattern becomes apparent. This vertical distortion becomes more pronounced over time. Experimentally

determined maximum vertical radius during pre-collapse and distorted value of radius are shown in Figure S6e-f, respectively. The observed relative shift in the SSPM diffraction ring was attributed to heat convection. The quantification of this distortion is achieved in terms of the nonlinear refractive index, as described by Equation 26. This distortion index, expressed as $^{\Delta n_2/n_2}$, increases with the increment of the value of intensity. Distortion index ($^{\Delta n_2/n_2}$) is quantified in percentage for three laser beams with wavelengths (λ) values of 650, 532, and 405 nm as shown in Figure S6g. The distortion or relative nonlinear refractive index is found to be 62.16 % (650 nm), 66.41% (532 nm), and 46.48% (405 nm) for intensities 10.318 W.cm^{-2}, 5.39 W.cm^{-2}, and 1.244 W.cm^{-2}. The 532 nm laser induces greater distortion than the 650 nm laser at similar intensities, because each photon in the 532 nm beam has greater energy than those in the 650 nm beam. The extent of distortion caused by 405 nm is the most significant. However, the distortion increases to a peak once the laser beam's intensity exceeds a specific threshold.

Section S6. Electronic Relationship Between $\chi^{(3)}_{monolayer}$, Mobility (μ), and Effective Mass (m^*)

In addition, an experiment is conducted to determine the source of the SSPM pattern generation by establishing a correlation between $\chi^{(3)}$ and mobility, as well as $\chi^{(3)}$ and effective mass. Hu et al. introduced a technique to establish relationships between electronic coherence phenomena and carrier mobility and effective mass.[42] Carrier mobility denotes the ability of a carrier to react to an external electric field through movement. The dynamics of the carrier within the ab plane of the unit cell are influenced by the effective mass and the dispersion characteristics of the carrier. The high value of $\chi^{(3)}_{monolayer}$ is a consequence of the reduced presence of electron scattering in the 2D material. Therefore, based on this reasoning, the optical coefficient $\chi^{(3)}$ is associated with electrical characteristics such as effective mass (m^*) and carrier mobility *(μ)*. In this study, we have investigated a correlation between the value of $\chi^{(3)}$ acquired from the SSPM experiment and the values of mobility and effective mass of 2D Bi_2Te_3 as reported in the relevant literature.[80] The value of other included materials is taken from relevant literature, also the value of the μ and m^* are derived from the Supporting Information in Table S3. The reported value of $\chi^{(3)}$ (10^{-7} e.s.u.) and its relationship to electronic activity is better than that of Graphene, as shown in Figures S7a and S7b. It may be inferred from Figure S6b that the carrier type of the semiconductor nanostructure can be identified using Equation 28. The relationship in the term can be expressed as, $\chi^{(3)}$ vs μ and $\chi^{(3)}$ vs m^*,[30] i.e.

$$\chi^{(3)} = 8.00/\sqrt{m^*} \quad \text{..... (27)}$$

And,

$$\chi^{(3)} = 0.146 \times \sqrt{\mu} \quad \ldots\ldots\ldots\ldots\ldots\ldots\ldots\ldots \quad (28)$$

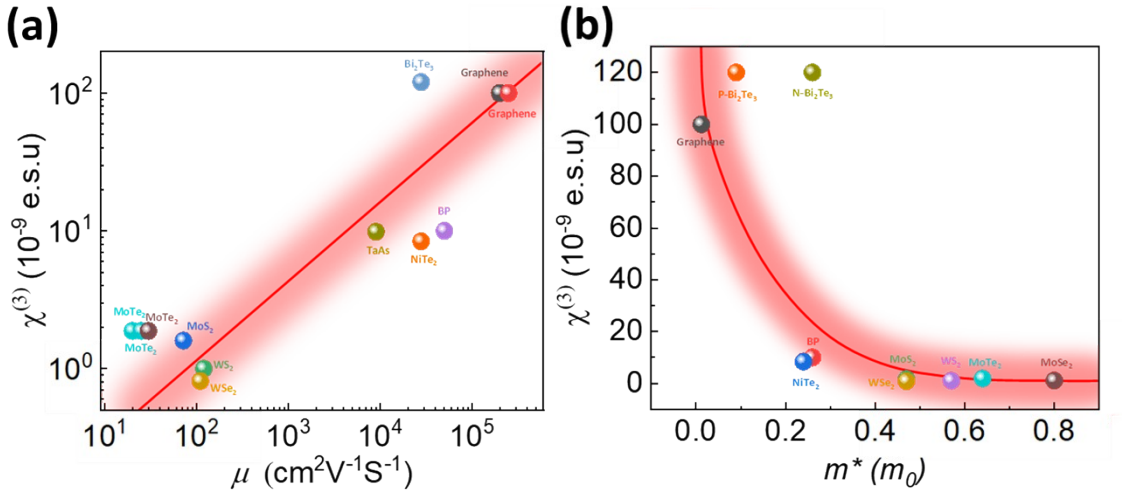

Figure S7. Comparative study between optical and electronic coefficients. (a) $\chi^{(3)}(10^{-9}\, e.s.u)$ versus μ. (b) $\chi^{(3)}(10^{-9}\, e.s.u)$ versus effective mass (m^*) of several 2D materials

Table S3: The values of $\chi^{(3)}$, Mobility (μ) & Effective Mass (m^*)

Material & Corresponding Wavelength	$\chi^{(3)}_{monolayer}$ (Third-order nonlinear susceptibility)	Mobility (μ) & Effective Mass (m^*)	Reference
Graphene	1×10^{-3} (e.s.u.)	81, 82	30, 75
BP	10^{-5} (e.s.u.)	83, 84	31
MoS_2	1.44×10^{-4} (e.s.u.)	85	32
WSe_2	1.371×10^{-6}/ 4.04×10^{-6} /2.98×10^{-6} (e.s.u.)	86	29
TaAs (405 nm/ 532 nm/ 671 nm/ 841 nm)	6.06×10^{-4} / 5.68×10^{-4} / 5.30×10^{-4}/ 4.65×10^{-4} (e.s.u.)/ 6.06×10^{-4} / 5.68×10^{-4} / 5.30×10^{-4}/ 4.65×10^{-4} (e.s.u.)	51	51
$MoSe_2$ (532 nm)	1.76×10^{-4} (e.s.u.)	87	36
WS_2	8.14×10^{-10}/ 8.44×10^{-11} / 3.69×10^{-9} (e.s.u.)	88	77
$MoTe_2$	1.88×10^{-9} (e.s.u.) 1.3×10^{-9} (e.s.u.) 1.14×10^{-9} (e.s.u.) 0.98×10^{-9} (e.s.u.) (CW 473 nm /532 nm/ 750 nm/ 801 nm)	89	42

Section S7:

This study focuses on the nonlinear optical properties of 2D Bi_2Te_3 using SSPM Spectroscopy. The light source used in the SSPM experiment is a continuous-wave laser. According to recent findings, the SSPM does not arise from the thermally induced response. The following paragraphs will elaborate on the supporting arguments. In the Supporting Information Section S6 Electronic Relation between $\chi^{(3)}_{monolayer}$), Mobility (μ), and Effective Mass (m^*), we have examined the relationship between effective mass and carrier mobility. The mobility of the carrier is characterized by its capacity to traverse in the presence of an external field. This relies on the carrier's effective mass and scattering behavior. In the third-order nonlinear optical response, the mobility of carriers within the coherent laser field establishes ac nonlocal electronic coherence. Hu et al.[42] anticipated that $\chi^{(3)}_{monolayer}$ shows a positive correlation with carrier mobility. Both parameters indicate the ability to store charge, reflecting the dissipative characteristic and highlighting the mechanism by which energy is dissipated within the carrier mass. The effective mass captures a dissipative characteristic, highlighting the mechanism by which energy is dissipated. The light field improves the motion of the carriers, resulting in reduced scattering during their movement, which leads to a higher value of $\chi^{(3)}_{monolayer}$. The elevated value of $\chi^{(3)}_{monolayer}$ rises as the wavelength decreases, corresponding to an increase in photon energy with shorter wavelengths. The main manuscript presents a summary of the values

of $\chi^{(3)}_{monolayer}$ assessed using the SSPM Spectroscopy method in relation to carrier mobility μ and effective mass m^*. $\chi^{(3)}_{monolayer}$ represents an optical parameter, μ denotes an electronic property, and m^* pertains to the electronic structure in the excited state. The relationship between optical properties and electronic properties reinforces the phenomenon of laser-induced coherence.

In addition to the Kerr nonlinearity, fluctuations in the medium's temperature caused by a powerful laser beam can modify the refractive index, leading to effects akin to self-phase modulation as documented earlier. Dabby et al.[90] characterized this phenomenon as the "thermal lens effect." The study we have conducted focuses on the "Wind Chime Model," which relies on the polarization of suspended nanostructures and their subsequent reorientation when subjected to a laser beam. The thermal lens effect demonstrates a linear optical response.[91] The mechanical chopper is utilized to validate the previously stated assertion. Figure S8a illustrates the optical configuration that includes a mechanical chopper. The chopper is first operated within a frequency range of 50 to 200 Hz (50 Hz interval) at an intensity of 11.45 W/cm². At the same intensity, the chopper was run at a higher frequency of 0.5-3.75 kHz (250 Hz interval) to examine the variation in the number of rings; however, no significant change was seen. At high chopping frequencies (0.5-3.75 kHz), no change in the number of rings is observed, indicating a similar level of electronic excitation. This same experiment was performed for lower frequencies, 50-200 Hz (with a 25 Hz step increment). Even in lower frequencies of the mechanical chopper, no change in the number of rings of the diffraction pattern was observed with increasing frequency. Therefore, we may conclude that electronic coherence, which induces a nonlinear optical response, predominates over the thermal lens effect.

The thermal camera was used to record the thermal profile at the same intensity, as in the configuration illustrated in Figure S9a, at different frequencies. The thermal interaction of the laser with the solvent is measured at various chopping frequencies, where the emergence of the "Thermal lens effect" is anticipated. The temperature difference is measured before and after laser impact at 0, 1, and 2 kHz. Figure S9b①, c①, d①, and e① illustrate the upper view of the cuvette prior to laser impact at frequencies of 0 kHz, 1 kHz, and 2 kHz, respectively. Figures S9b②, c②, d②, and e② illustrate the upper view of the cuvette following laser impact at frequencies of 0, 0.5, 2, and 3.5 kHz, respectively. Figure S9g presents the temperature difference before and after laser impact, including the chopper frequency. As the chopping frequency increases, the interaction between the laser and the solvent diminishes, leading to reduced localized solvent heating. A decrease in temperature is observed with increasing chopping frequency. After each increase of 0.25 kHz in the chopping frequency, a decrease in

the temperature difference was observed. The number of rings remains constant despite the increase in chopping frequency, as illustrated in Figure S8b ①-⑮. The initial reduction in the number of rings is attributed to the diminished intensity of the laser beam, which decreases electronic coherence and results in fewer rings. The decrease in temperature did not alter the ring number, as illustrated in Figure S9f, indicating that the SSPM phenomenon is not thermally induced. The aforementioned statements offer a comprehensive rationale indicating that SSPM is not a thermally induced phenomenon resulting from the “thermal lens effect”.

A similar experiment was performed at 532 nm to determine whether the previously drawn conclusion also applies here. The thermal interaction between the laser and the solvent is assessed at different chopping frequencies, where the "Thermal lens effect" is expected. The temperature variation is assessed before and after laser application at 0, 1, and 2 kHz. Figures S11a①, b①, c①, and d① show the top view of the cuvette before laser exposure at frequencies of 0 kHz, 1 kHz, and 2 kHz, respectively. Figures S11a②, b②, c②, and d② show the superior perspective of the cuvette after laser exposure at 0, 0.5, 2, and 3.5 kHz, respectively. Figure S11f illustrates the temperature differential measured before and after laser application, including chopper frequency. As the chopping frequency increases, contact between the laser and the solvent decreases, reducing solvent heating. Although the temperature difference decreased, the number of rings remained the same, as shown in Figure S11e. The number of rings with variable chopping frequency is shown in Figure S9, with chopping frequencies ranging from 0 to 3.75 kHz at 250 Hz intervals.

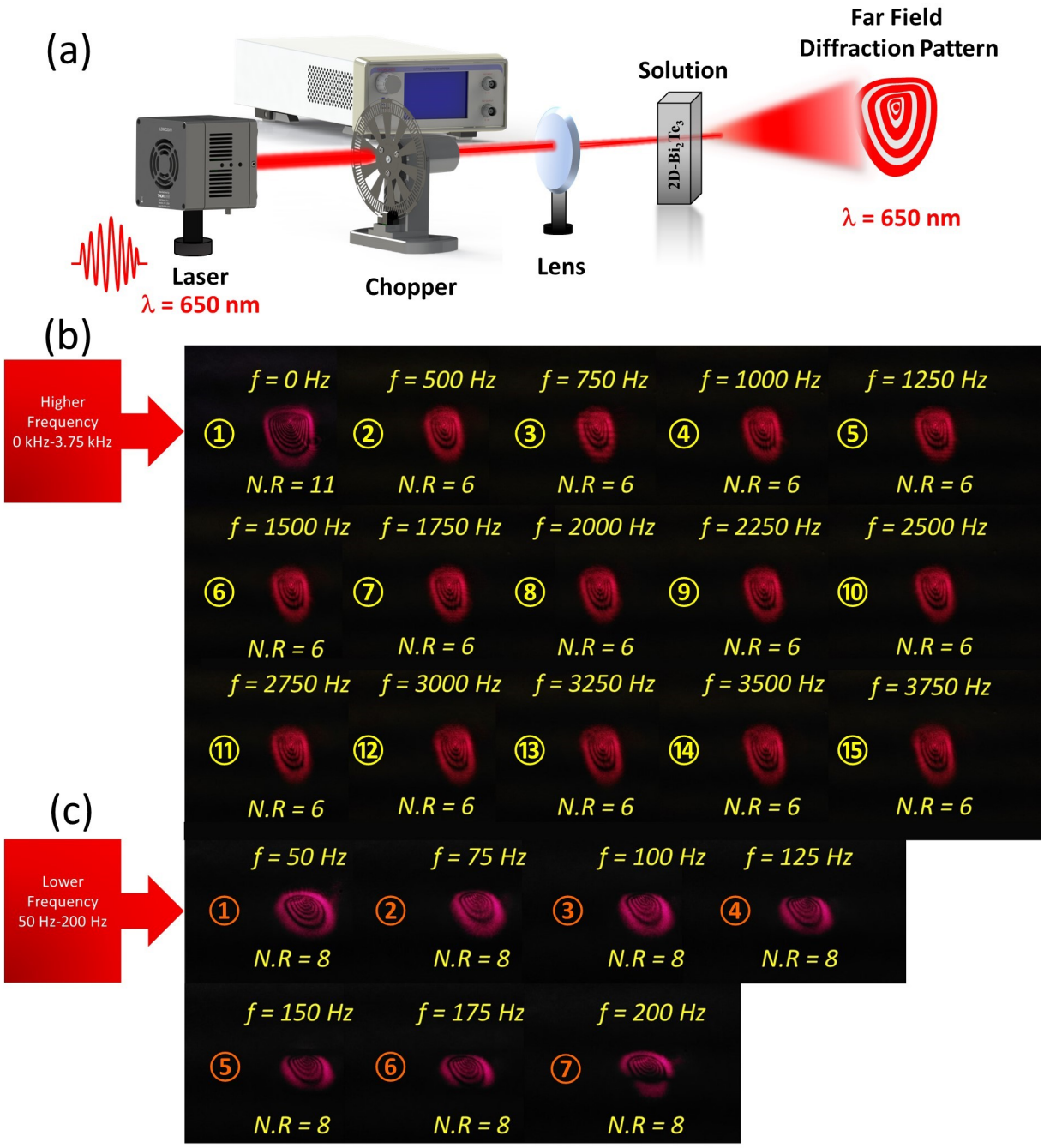

Figure S8. (a) Schematic representation of the SSPM setup. (b-c) mechanical chopper operating between high Frequency (0.5-3.75 kHz) and low frequency (0-200 Hz).

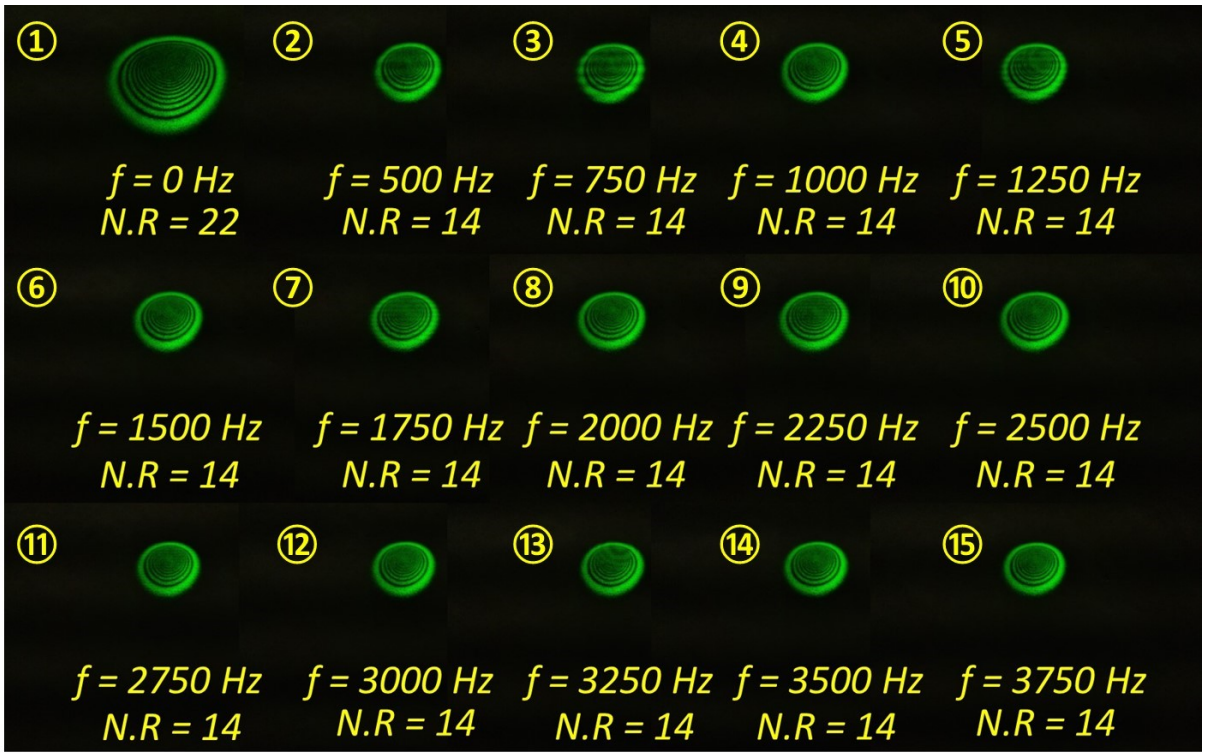

Figure S9. Mechanical chopper operating at high Frequency for 532 nm. (0-3.75 kHz).

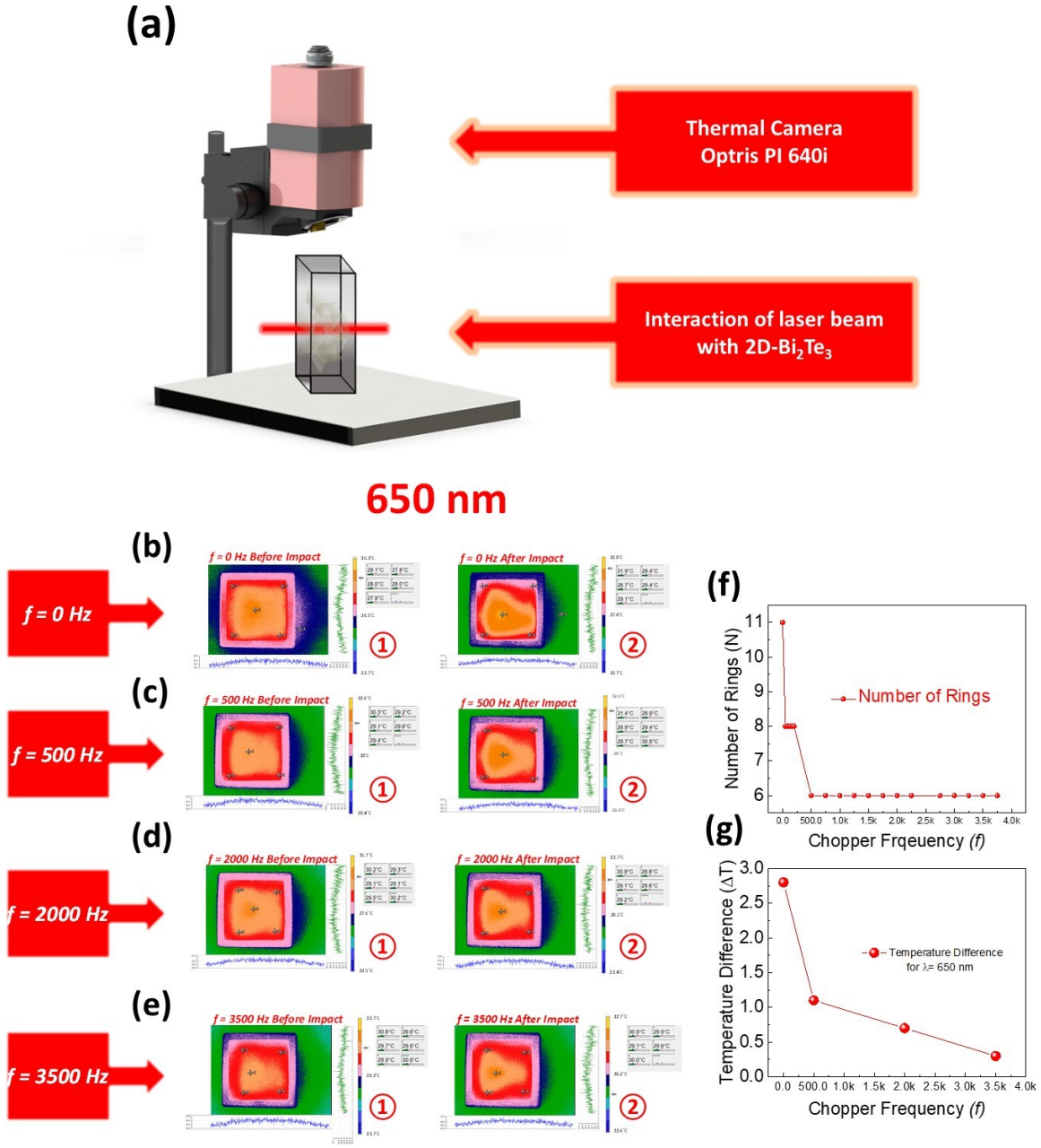

Figure S10. (a) Thermal camera setup for measuring the upper view of the cuvette's thermal profile. (b)- (c) -(d)- (e) Thermal profile of the cuvette before and after the laser impact for frequencies 0 kHz, 500 Hz, 2 kHz, and 3.5 kHz at wavelength 650 nm. (f) Number of Rings vs frequency of the mechanical chopper. (g) The temperature difference before and after the laser impact of the incoming laser beam.

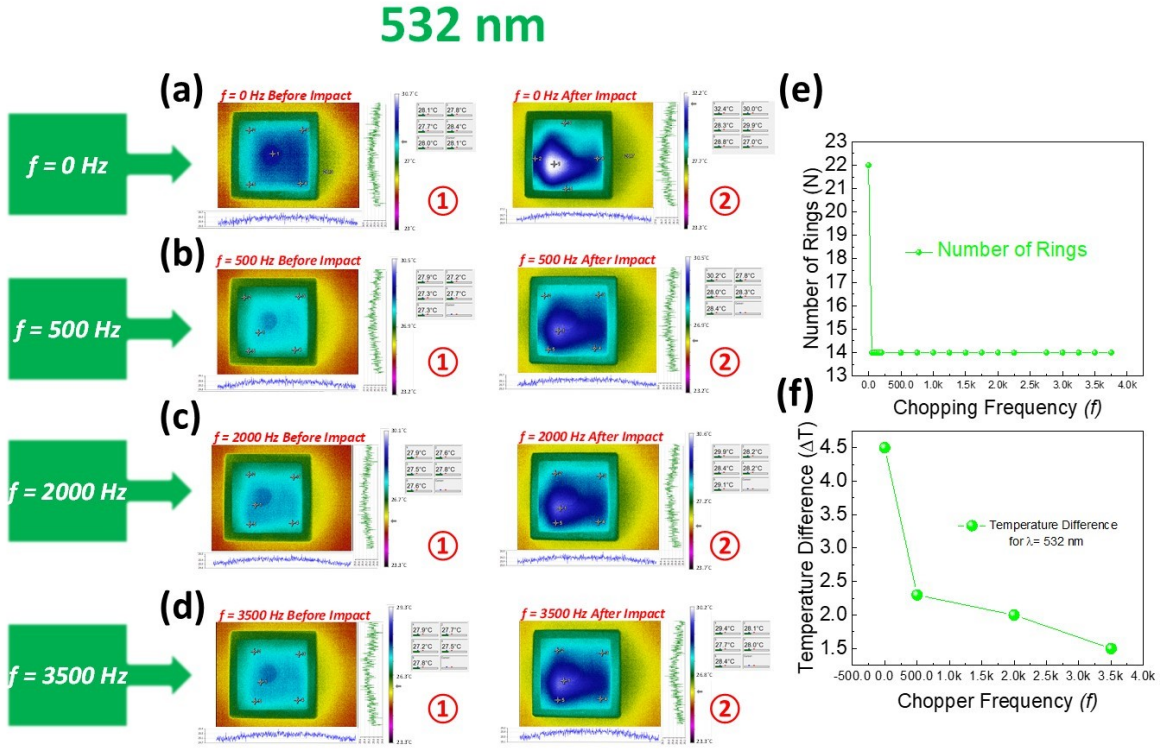

Figure S11. (a)-(b)- (c) -(d) Thermal profile of the cuvette before and after the laser impact for frequencies 0 kHz, 500 Hz, 2 kHz, and 3.5 kHz at wavelength 532 nm. (e) Number of Rings vs frequency of the mechanical chopper. (f) The temperature difference before and after the laser impact of the incoming laser beam for a wavelength of 532 nm.

Section S8: The bandgap calculation of 2D-hBN using the Tauc method

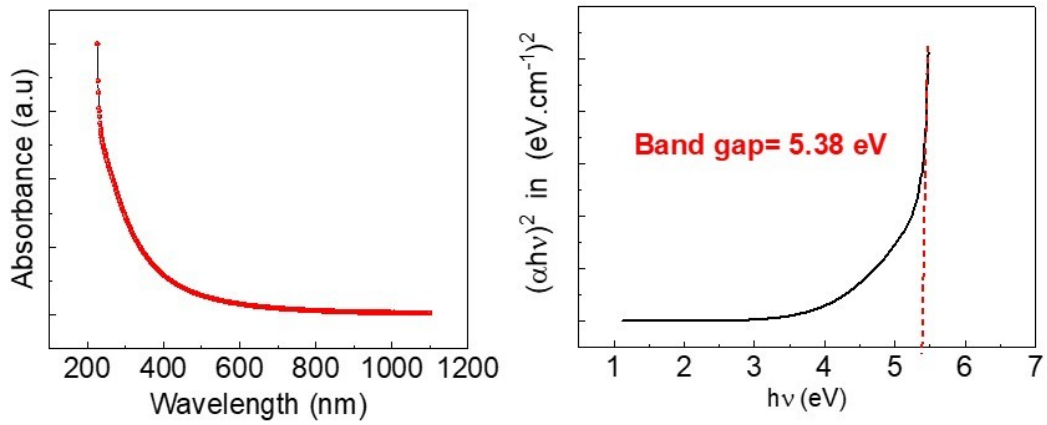

Figure S12. (a) showing the absorbance spectrum of the 2D-hBN derived from UV-vis Spectroscopy. Figure (b) shows the determined value of the direct bandgap 5.38 eV using the Tauc plot.

Section S9: Laser Beam Solvent Control Experiment

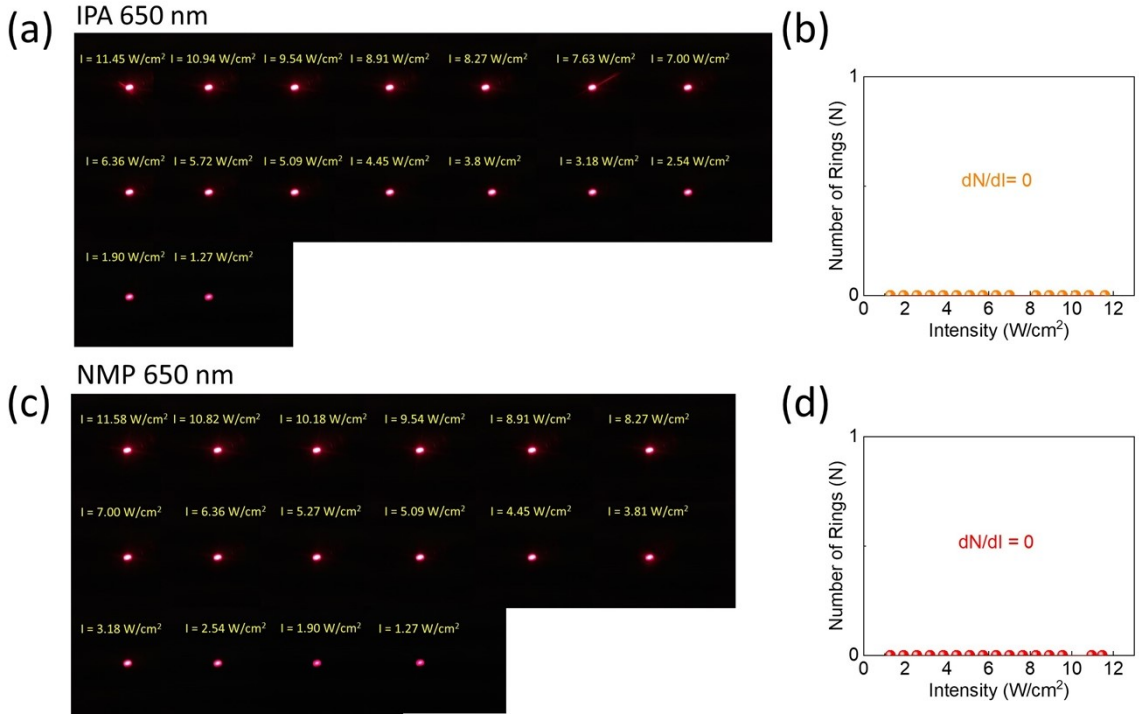

Figure S13. (a) An outgoing laser beam was recorded on the far screen after the interaction between the laser beam and IPA. (b) corresponding value of dN/dI calculated through the IPA-laser control experiment. (c) Outgoing laser beam recorded at the far-screen after the laser beam and NMP interaction. (d) corresponding value of dN/dI calculated through the experiment, NMP-laser control experiment.

Section S10: The Similar Comparison Method- n_2 estimation

The Similar Comparison Method has been implemented to enhance the selection of specific wavelengths (650, 532, and 405 nm). Recent reports indicate the utilization of wavelengths 671, 532, 457, and 405 nm for a similar comparison method. A comparable method can be employed to determine the value of n_2 for Bi_2Te_3-based photonic diodes and other analogous semiconducting nanostructures, where nonreciprocal light propagation has been realized. The nonlinear refractive index can be defined as,

$$n_2 = \frac{\lambda}{2n_0 L_{eff}} \cdot \frac{dN}{dI}$$

Here, $\lambda/2n_0L_{eff}$ is a constant, λ, n_0, L_{eff} are the wavelength of the incoming laser beam, linear refractive index, and effective optical path length of the incoming laser beam inside the cuvette. Estimating the nonlinear refractive index of a 2D Bi_2Te_3-based photonic diode requires a

comparative analysis with other materials that have well-established nonlinear refractive indices.

Similar contrast (S) is defined as,

$$S = 1 - D = \frac{|n_{21} - n_{22}|}{n_{21}}$$

$$S = 1 - \frac{\left|\frac{\lambda}{2n_0 L_{eff}}\frac{N_1}{I_1} - \frac{\lambda}{2n_0 L_{eff}}\frac{N_2}{I_2}\right|}{\frac{\lambda}{2n_0 L_{eff}}\frac{N_1}{I_1}} = 1 - \frac{\left|\frac{N_1}{I_1} - \frac{N_2}{I_2}\right|}{\frac{N_1}{I_1}}$$

D denotes the difference contrast, while n_{21} and n_{22} signify the nonlinear refractive indices of the heterostructure under forward- and reverse-bias conditions, respectively. The contrast is measured relative to other 2D materials, with the coefficients for the 2D materials documented in Table S8.

Table S8: The value of material, nonlinear index, and Similar contrast calculated using SSPM Spectroscopy.

Material	Nonlinear Refractive Index (cm^2W^{-1})	Similar Contrast (%)	Reference
MoS_2	$\approx 10^{-7}$	74%	77
Bi_2Se_3	$\approx 10^{-9}$	58%	44
SnS	$\approx 10^{-5}$	90%	48
Sb	$\approx 10^{-6}$	85%	39
Graphdiyne	$\approx 10^{-5}$	92%	33
CuPc	$\approx 10^{-6}$	75%	36
Graphene	$\approx 10^{-5}$	95%	36
SnS_2	$\approx 10^{-9}$	54%	33
$NiTe_2$	$\approx 10^{-5}$	91.8%	92
Bi_2Te_3	$\approx 10^{-4}$	98.3%	

Figure S14 indicates that the 2D $NiTe_2$ demonstrates a nonlinear refractive index similar to that of Sb and SnS, with a n_2 range of 10^{-5} $cm^2.W^{-1}$. This was previously validated through experimentation using SSPM spectroscopy. This demonstrates the reliability and repeatability of the SSPM experiment. The 2D-Bi_2Te_3 demonstrates a significant contrast of approximately 98.3%.

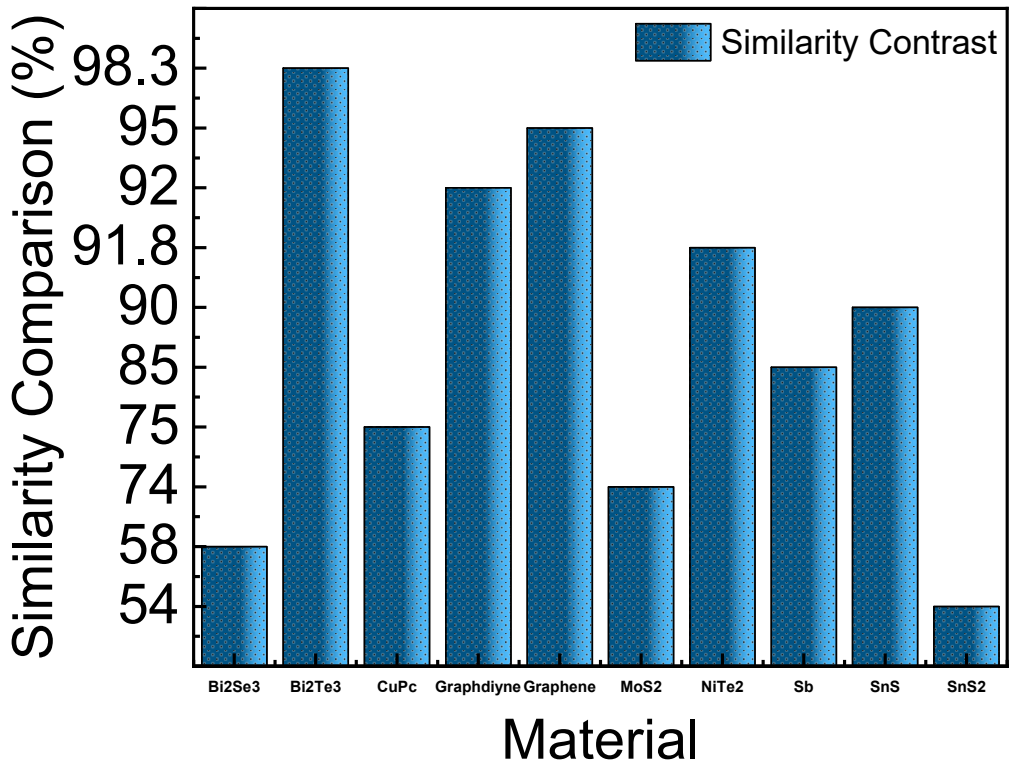

Figure S14: Similarity comparison method for n_2 estimation in all photonic diodes.

Section S11: Intensity Dependent Dynamic Collapse of Diffraction Pattern and Variation in Nonlinear Refractive Index with Different Solvents

The previous section discussed the time evolution of diffraction patterns at different laser beam wavelengths and solvents. Supporting Information Section S5 shows the intensity-dependent dynamic collapse of the diffraction pattern and change in the nonlinear refractive index for different wavelengths (λ = 650, 532, and 405 nm). Here, the dynamics of the collapse phenomenon in different solvents are discussed. Figure S15a(①-②) shows the pre- and post-collapse images of the diffraction pattern for the 2D Bi_2Te_3-IPA system at wavelength 650 nm, concentration C_2, and L =10 mm. Figure 4b shows the progression of the vertical and horizontal diameters with time at a wavelength of λ= 650 nm, in IPA solvent. The Figures S15c and S15d show $\frac{\Delta n_2}{n_2}\%$ distortion for the IPA and NMP solvents, respectively.

The absorbed laser energy leads to a gradual increase in solvent temperature, attributed to thermal effects. Laser heating induces convection, with an upward current in the central region

of the beam that helps flatten the temperature gradient profile in the upper section of the heated region.[93] This results in a reduction in 2D nanostructures in the upper section of the cuvette volume, thereby decreasing light-matter interactions in the upper area relative to the lower one, along the laser beam path. The upper portion of the diffraction pattern is distorted compared to the lower region. Consequently, thermal action induces density variations that depend on the temperature of the liquid sample. This density gradient generates the spatial distribution of the buoyant force inside the solvent. The movement of the liquid layers transfers heat from the region of the concentrated light beam to the surrounding area.

While some authors have previously proposed the concept, there is currently no extant experimental evidence supporting such an experiment.[94] Previously, it was concluded that the IPA-2D Bi_2Te_3 interface experiences less frictional force compared to the NMP-2D Bi_2Te_3 one. This lower frictional force should make the convection current faster in IPA than in NMP. In contrast, the entire collapse process for IPA takes 0.9666 s, as shown in Figure S15b, whereas that for NMP takes only 0.6666 s. Thus, it is observed that fluid convection is more significant in the case of NMP-2D Bi_2Te_3 compared to IPA-2D Bi_2Te_3. As the amount of volume of 2D Bi_2Te_3 is smaller than the volume of the solvent, the characteristics of the solvent become dominant in the convection process. The temperature gradient was monitored using an Optris PI 640i infrared camera in the optical setup shown in Figure S15e. The thermal convection flow within the cuvette is anticipated to follow the behavior depicted in Figure S15f. The analysis indicates that the heat-releasing process is more significant for the NMP method, resulting in a more uniform temperature gradient at the upper section of the solvent. Figure S15g depicts a shift in the vertical temperature difference before and after laser illumination in the IPA-2D Bi_2Te_3 solution. Figure S15h(①-②) shows the temperature map before and after laser illumination at 73 mW, at the wavelength (λ) of 650 nm. Figure S15i illustrates the vertical temperature profile change before and after laser illumination in NMP-2D Bi_2Te_3 solution. Figure S15j(①-②), taken at 71 mW, shows the temperature profile of the surface for the NMP-2D Bi_2Te_3 solution. A higher temperature gradient is observed compared to the IPA-2D Bi_2Te_3 solution, as shown in Figure S15j(①-②). Figures S15h(①-②) and S15j(①-②) capture snapshots of the surface temperature profile, although the temperature profile in the solvent where the beam is projected differs. Figure S15j(①-②) shows a higher temperature gradient than Figure S15h(①-②). The same is seen in Figures S15i-g. IPA[95] [161.2 ($J\ mol^{-1}K^{-1}$)] has a lower specific heat than NMP[96] [412.4 ($J\ mol^{-1}K^{-1}$)], so the temperature at the beam focal point is higher for IPA-2D Bi_2Te_3 than for NMP-2D Bi_2Te_3. Figure S15j(②) shows a different temperature profile map compared to Figure S15h(②). In contrast, the temperature at which

the beam is focused is higher for the IPA-2D Bi_2Te_3 system than for the NMP-2D Bi_2Te_3 system. From these observations, we conclude that the heat exchange capacity of NMP-2D Bi_2Te_3 is greater than that of IPA-2D Bi_2Te_3, as a smaller temperature difference between the focal point and the top surface of the liquid is observed in the latter case.

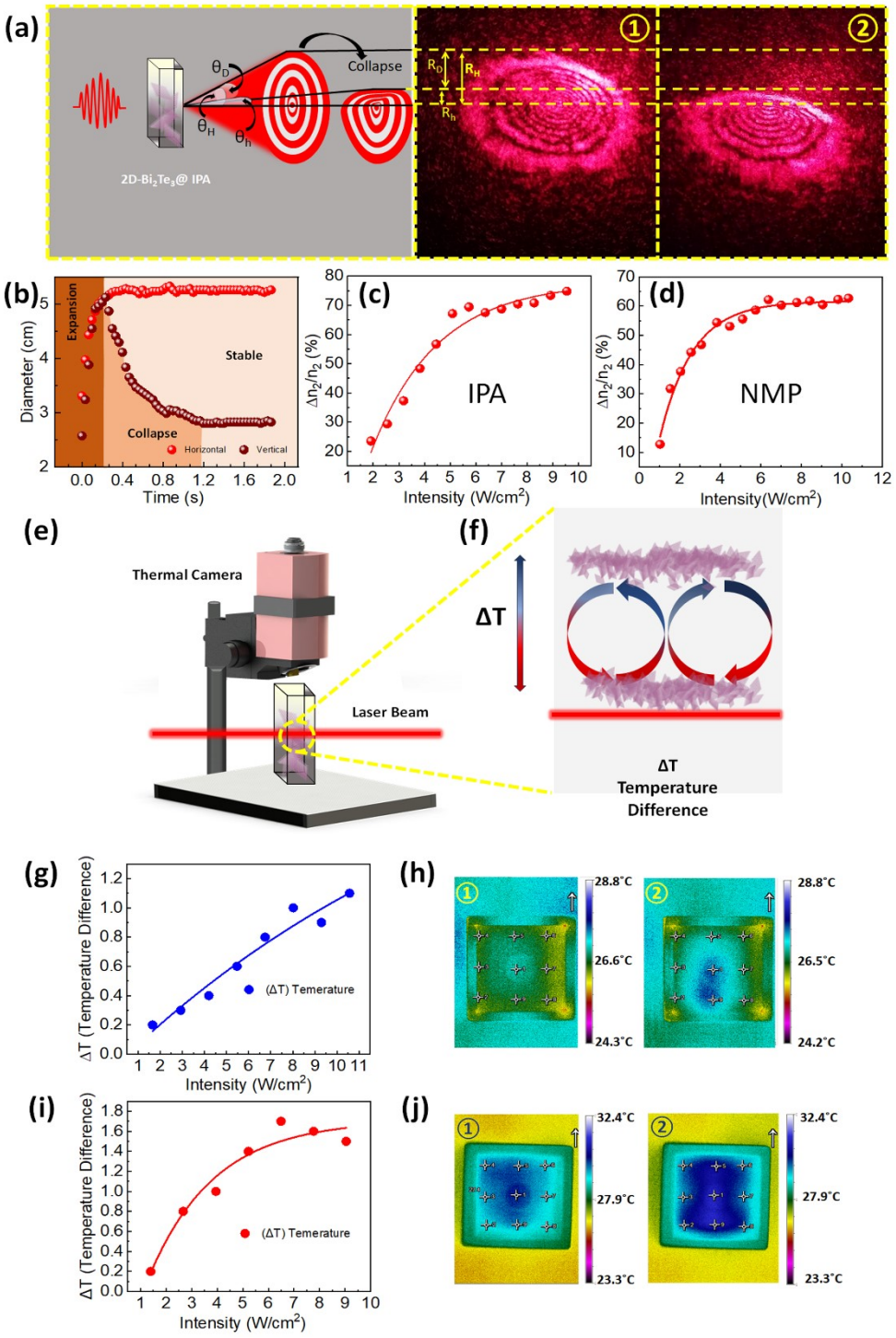

Figure S15. (a) Illustration of the collapse phenomenon of the SSPM diffraction pattern featuring a semi-cone and distortion angle for 2D Bi_2Te_3 in IPA solvent. (b) The progression of the vertical diameter and horizontal diameter

with time at a wavelength (λ) of 650 nm in IPA solvent. (c-d) The distortion of the refractive index ($^{\Delta n_2/n_2)\%}$ as recorded in the far field for 650 nm in IPA and NMP. (e) Thermal camera setup to visualize the temperature profile of the top surface. (f) Thermal convection is induced by laser heating of the solvent. (g) Temperature difference before and after laser impact of the laser beam with respect to intensity for IPA solvent. (h) ①-② Temperature profile of the top surface of the solvent in the cuvette before and after laser beam impact for IPA solvent at an intensity of 73 mW. (i) Temperature difference before and after the impact of the laser beam with respect to intensity for NMP solvent. (j) ①-② Temperature profile of the top surface of the solvent in the cuvette before and after the laser beam impact for NMP solvent at an intensity of 71 mW.

The convection velocity is linearly dependent on ΔT, as the fluid tends to flow from the high-density/high-temperature region to the low-density/low-temperature region, thereby driving the convection. NMP has lower viscosity than the IPA solvent, which aids the NMP system in this convection process (here, the 2D Bi_2Te_3-NMP system is not mentioned; only solvent characteristics are highlighted). This convection velocity causes the distortion, as shown in Figure S15a (①-②). From the experiment, it was verified that $\frac{\Delta n_2}{n_2}\%$ is more pronounced in the case of IPA-2D Bi_2Te_3 solution, compared to NMP-2D Bi_2Te_3. Figure S15c shows the variation of $\frac{\Delta n_2}{n_2}\%$ with varying intensity for NMP-2D Bi_2Te_3 solution, we can see a saturating behavior after a threshold intensity (6.36 Wcm^{-2}). The distortion can also be compared with Figures S15b and S5b, where for the same laser beam intensity IPA- 2D Bi_2Te_3 system shows greater collapse in the vertical diameter. The same conclusion can be drawn from the top-surface temperature profile in Figure S15i. This leads to the conclusion that the convection velocity becomes fixed after a certain threshold. However, IPA-2D Bi_2Te_3 does not exhibit saturating behavior, as shown in Figure S15g. High viscosity leads to more distortion in diffraction patterns and non-saturating behavior, as seen in Figure S15g. The thermal conductivity of NMP is higher than that of IPA, allowing the fluid to reach a more uniform, stable condition faster.

Table S9: Nonlinear Optical Coefficients of reported isolators calculated using SSPM Spectroscopy.

Sample Name	(dN/dI) -405	(dN/dI)-457	(dN/dI)-473	(dN/dI) -532	(dN/dI) - 633	(dN/dI) - 650	(dN/dI)- 671	$\chi^{(3)}_{total}$-405	$\chi^{(3)}_{total}$- 473	$\chi^{(3)}_{total}$- 532	$\chi^{(3)}_{total}$ -650	$\chi^{(3)}_{total}$ -671	Range	n_2 – 532 nm	Citation
$(PPA)_3BiI_6$-SnS_2	0.192	--	0.117	0.064	--	--	--	1.77×10^{-8} (e.s.u.)	1.26×10^{-8} (e.s.u.)	7.74×10^{-9} (e.s.u.)	--	--	25-225	--	54
2D $NiTe_2$-2D hBN	5.06	--	--	2.96	--	1.22	--	3.76×10^{-3}	3.76×10^{-3}	2.99×10^{-3}	1.56×10^{-3},	--	0-8	--	52
2D Te- 2D hBN	--	0.458	--	.331	--	--	0.26	--	--	--		--	0-60	6.202×10^{-5}	38
InP-SnS2	--	--	--	--	--	--	--	--	--	--	--	--	25-225	1.18×10^{-6}	97
InSe-gC_3N_4	--	0.284	--	0.081	--	--	0.016	--	--	--	--	--	30-150	3.04×10^{-5}	5
$MoSe_2$-SnS_2	--	--	--	1.479	--	--	0.9816	0.01537	--	0.00706 (e.s.u.)		0.00428 (e.s.u.)	0-12	1.3×10^{-5}	36
2D Graphidyne-2D SnS_2	--	--	--	0.11	--	--	0.04	--	--	--	--	--	0-60	--	33
porphyrin–napthalimide molecules	--	4.5	--	3.2	1.28	--	--	--	--	6.8×10^{-2} (e.s.u.)	0.45×10^{-2}	--	2-11	0.49×10^{-4}	98
$Ge_{25}Sb_5Se_{70}$ chalcogenide glass- TiO_2	--	--	--	--	--	--	--	--	--	--	--	--	14-100	5.50×10^{-5} cm^2/W.	99
DAAQ-TFP COF-CeO2	4.039	--	--	1.37	--	--	--	2.39×10^{-3} (e.s.u.)	--	1.37×10^{-3} (e.s.u.)	--	--	2-13	2.506×10^{-5} cm^2/W.	100
CuPc-SnS_2	--	--	--	1.41	--	--	1.12	--	--	2.01×10^{-3} (e.s.u.)	--	--	2-11	2.65×10^{-5} cm^2/W.	101
Mn_3O_4-TiO_2	--	--	--	--	--	--	--	--	--	--	--	--	20-100	4.87×10^{-6} cm^2/W	102
$RbPbI_3$-SnS_2	--	--	--	2.59	--	--	--	--	--	0.003	--	--	1-4	2.16×10^{-5} cm^2/W	103
MoS_2-hBN	--	--	--	--	--	--	--	--	--	--	--	--	2-50		104
SnS_2-Bi_2Se_3 (671 nm)/	7.24×10^{-3} e.s.u.	--	--		--	--	-- 4.19458	--	--	--	--	--	(2.64-8.47)	2.53×10^{-5} cm^2/W	105

References

1. T. Sharifi, S. Yazdi, G. Costin, A. Apte, G. Coulter, C. Tiwary and P. M. Ajayan, *Chemistry of Materials*, 2018, **30**, 6108-6115.
2. H. M. Rietveld, *Applied Crystallography*, 1969, **2**, 65-71.
3. P. Ngabonziza, R. Heimbuch, N. De Jong, R. Klaassen, M. Stehno, M. Snelder, A. Solmaz, S. Ramankutty, E. Frantzeskakis and E. Van Heumen, *Physical Review B*, 2015, **92**, 035405.
4. L. A. Reyes-Verdugo, M. d. J. Martinez-Carreon, C. Gutierrez-Lazos, F. J. Solis-Pomar, J. G. Quiñones-Galvan and E. Perez-Tijerina, *Journal of Nanotechnology*, 2024, **2024**, 6623255.
5. R. Galceran, F. Bonell, L. Camosi, G. Sauthier, Z. M. Gebeyehu, M. J. Esplandiu, A. Arrighi, I. Fernández Aguirre, A. I. Figueroa and J. F. Sierra, *Advanced Materials Interfaces*, 2022, **9**, 2201997.
6. P. Ngabonziza, M. P. Stehno, H. Myoren, V. A. Neumann, G. Koster and A. Brinkman, *Advanced electronic materials*, 2016, **2**, 1600157.
7. X. Zhang, X. Liu, C. Zhang, S. Peng, H. Zhou, L. He, J. Gou, X. Wang and J. Wang, *ACS nano*, 2022, **16**, 4851-4860.
8. J. Yadav, M. Anoop, N. Yadav, N. S. Rao, F. Singh, T. Ichikawa, A. Jain, K. Awasthi, R. Singh and M. Kumar, *Journal of Materials Science: Materials in Electronics*, 2023, **34**, 175.
9. B. Trawiński, B. Bochentyn, M. Łapiński and B. Kusz, *Thermochimica Acta*, 2020, **683**, 178437.
10. H. Bando, K. Koizumi, Y. Oikawa, K. Daikohara, V. Kulbachinskii and H. Ozaki, *Journal of Physics: Condensed Matter*, 2000, **12**, 5607.
11. P. Kumar, P. Srivastava, J. Singh, R. Belwal, M. K. Pandey, K. Hui, K. Hui and K. Singh, *Journal of Physics D: Applied Physics*, 2013, **46**, 285301.
12. M. Ahmad, K. Agarwal and B. Mehta, *Journal of Applied Physics*, 2020, **128**.
13. S. M. Abzal, S. L. Janga, Y. Bhaskara Rao, S. Khatua, K. Kalyan, P. Maiti, R. Patel, L. N. Patro and J. K. Dash, *Journal of Materials Science*, 2024, **59**, 6879-6893.
14. B. Long, Z. Qiao, J. Zhang, S. Zhang, M.-S. Balogun, J. Lu, S. Song and Y. Tong, *Journal of Materials Chemistry A*, 2019, **7**, 11370-11378.
15. A. Ghosh, S. Shukla, M. Monisha, A. Kumar, B. Lochab and S. Mitra, *ACS Energy Letters*, 2017, **2**, 2478-2485.
16. E. A. Hoffmann, T. Körtvélyesi, E. Wilusz, L. S. Korugic-Karasz, F. E. Karasz and Z. A. Fekete, *Journal of Molecular Structure: THEOCHEM*, 2005, **725**, 5-8.
17. R. Zheng, W. Cheng, E. Wang and S. Dong, *Chemical physics letters*, 2004, **395**, 302-305.
18. D. Teweldebrhan, V. Goyal and A. A. Balandin, *Nano letters*, 2010, **10**, 1209-1218.
19. C. Wang, X. Zhu, L. Nilsson, J. Wen, G. Wang, X. Shan, Q. Zhang, S. Zhang, J. Jia and Q. Xue, *Nano Research*, 2013, **6**, 688-692.
20. W. Richter and C. Becker, *physica status solidi (b)*, 1977, **84**, 619-628.
21. H. Xu, Y. Song, Q. Gong, W. Pan, X. Wu and S. Wang, *Modern Physics Letters B*, 2015, **29**, 1550075.
22. V. Goyal, D. Teweldebrhan and A. A. Balandin, *Applied Physics Letters*, 2010, **97**.
23. G. D. Keskar, R. Podila, L. Zhang, A. M. Rao and L. D. Pfefferle, *The Journal of Physical Chemistry C*, 2013, **117**, 9446-9455.
24. M. Hajlaoui, E. Papalazarou, J. Mauchain, G. Lantz, N. Moisan, D. Boschetto, Z. Jiang, I. Miotkowski, Y. Chen and A. Taleb-Ibrahimi, *Nano letters*, 2012, **12**, 3532-3536.

25. Y. Zhao, X. Luo, J. Zhang, J. Wu, X. Bai, M. Wang, J. Jia, H. Peng, Z. Liu and S. Y. Quek, *Physical Review B*, 2014, **90**, 245428.
26. V. Wagner, G. Dolling, B. Powell and G. Landweher, *physica status solidi (b)*, 1978, **85**, 311-317.
27. Y. Liang, W. Wang, B. Zeng, G. Zhang, Y. Song, X. Zhang, J. Huang, J. Li and T. Li, *Solid State Communications*, 2011, **151**, 704-707.
28. W. G. Z. S. U. FA, *Appl. Phys. Lett*, 2014, **104**, 141909.
29. Y. Jia, Y. Shan, L. Wu, X. Dai, D. Fan and Y. Xiang, *Photonics Research*, 2018, **6**, 1040-1047.
30. R. Wu, Y. Zhang, S. Yan, F. Bian, W. Wang, X. Bai, X. Lu, J. Zhao and E. Wang, *Nano letters*, 2011, **11**, 5159-5164.
31. J. Zhang, X. Yu, W. Han, B. Lv, X. Li, S. Xiao, Y. Gao and J. He, *Optics letters*, 2016, **41**, 1704-1707.
32. Y. Wu, Q. Wu, F. Sun, C. Cheng, S. Meng and J. Zhao, *Proceedings of the National Academy of Sciences*, 2015, **112**, 11800-11805.
33. L. Wu, Y. Dong, J. Zhao, D. Ma, W. Huang, Y. Zhang, Y. Wang, X. Jiang, Y. Xiang and J. Li, *Adv. Mater.*, 2019, **31**, 1807981.
34. Y. Shan, L. Wu, Y. Liao, J. Tang, X. Dai and Y. Xiang, *Journal of Materials Chemistry C*, 2019, **7**, 3811-3816.
35. Y. Liao, Y. Shan, L. Wu, Y. Xiang and X. Dai, *Advanced Optical Materials*, 2020, **8**, 1901862.
36. K. Sk, B. Das, N. Chakraborty, M. Samanta, S. Bera, A. Bera, D. S. Roy, S. K. Pradhan, K. K. Chattopadhyay and M. Mondal, *Advanced Optical Materials*, 2022, **10**, 2200791.
37. L. Wu, X. Jiang, J. Zhao, W. Liang, Z. Li, W. Huang, Z. Lin, Y. Wang, F. Zhang and S. Lu, *Laser & Photonics Reviews*, 2018, **12**, 1870055.
38. L. Wu, W. Huang, Y. Wang, J. Zhao, D. Ma, Y. Xiang, J. Li, J. S. Ponraj, S. C. Dhanabalan and H. Zhang, *Advanced Functional Materials*, 2019, **29**, 1806346.
39. L. Lu, X. Tang, R. Cao, L. Wu, Z. Li, G. Jing, B. Dong, S. Lu, Y. Li and Y. Xiang, *Advanced Optical Materials*, 2017, **5**, 1700301.
40. B. Shi, L. Miao, Q. Wang, J. Du, P. Tang, J. Liu, C. Zhao and S. Wen, *Applied Physics Letters*, 2015, **107**.
41. Y. Shan, J. Tang, L. Wu, S. Lu, X. Dai and Y. Xiang, *Journal of Alloys and Compounds*, 2019, **771**, 900-904.
42. L. Hu, F. Sun, H. Zhao and J. Zhao, *Optics Letters*, 2019, **44**, 5214-5217.
43. Y. Jia, Y. Liao, L. Wu, Y. Shan, X. Dai, H. Cai, Y. Xiang and D. Fan, *Nanoscale*, 2019, **11**, 4515-4522.
44. X. Li, R. Liu, H. Xie, Y. Zhang, B. Lyu, P. Wang, J. Wang, Q. Fan, Y. Ma and S. Tao, *Optics Express*, 2017, **25**, 18346-18354.
45. Y. Liao, Q. Ma, Y. Shan, J. Liang, X. Dai and Y. Xiang, *Journal of Alloys and Compounds*, 2019, **806**, 999-1007.
46. Y. Jia, Z. Li, M. Saeed, J. Tang, H. Cai and Y. Xiang, *Optics Express*, 2019, **27**, 20857-20873.
47. C. Song, Y. Liao, Y. Xiang and X. Dai, *Science Bulletin*, 2020, **65**, 1030-1038.
48. L. Wu, Z. Xie, L. Lu, J. Zhao, Y. Wang, X. Jiang, Y. Ge, F. Zhang, S. Lu and Z. Guo, *Advanced Optical Materials*, 2018, **6**, 1700985.
49. Y. Shan, Z. Li, B. Ruan, J. Zhu, Y. Xiang and X. Dai, *Nanophotonics*, 2019, **8**, 2225-2234.
50. W. Wang, Y. Wu, Q. Wu, J. Hua and J. Zhao, *Scientific reports*, 2016, **6**, 22072.
51. Y. Huang, H. Zhao, Z. Li, L. Hu, Y. Wu, F. Sun, S. Meng and J. Zhao, *Advanced Materials*, 2023, **35**, 2208362.

52. S. Goswami, C. C. de Oliveira, B. Ipaves, P. L. Mahapatra, V. Pal, S. Sarkar, P. A. S. Autreto, S. K. Ray and C. S. Tiwary, *Laser & Photonics Reviews*, **n/a**, 2400999.
53. X. Xu, Z. Cui, Y. Yang, Y. Zhang, Q. Li, L. Tong, J. Li, X. Zhang and Y. Wu, *Laser & Photonics Reviews*, 2025, **19**, 2401521.
54. Z. Xu, H. Wang, W. Niu, Y. Guo, X. Zhai, P. Li, X. Zeng, S. Gull, J. Liu, J. Cao, X. Xu, G. Wen, G. Long, Y. Wu and J. Li, *Laser Photonics Rev.*, **n/a**, 2401929.
55. D. Weng, C. Ling, Y. Gao, G. Rui, L. Fan, Q. Cui, C. Xu and B. Gu, *Laser Photonics Rev.*, **n/a**, 2401587.
56. S. Bera, S. Kalimuddin, A. Bera, D. S. Roy, T. Debnath, S. Das and M. Mondal, *Adv. Opt. Mater.*, 2025, **13**, 2402318.
57. Y. Wu, L. Zhu, Q. Wu, F. Sun, J. Wei, Y. Tian, W. Wang, X. Bai, X. Zuo and J. Zhao, *Appl. Phys. Lett.*, 2016, **108**.
58. X. Xu, Z. Cui, Y. Yang, Y. Zhang, Q. Li, L. Tong, J. Li, X. Zhang and Y. Wu, *Laser Photonics Rev.*, 2025, **19**, 2401521.
59. J. Ridout and M. R. Probert, *CrystEngComm*, 2014, **16**, 7397-7400.
60. G. Müller, M. Lutz and S. Harder, *Structural Science*, 1996, **52**, 1014-1022.
61. N. Mounet, M. Gibertini, P. Schwaller, D. Campi, A. Merkys, A. Marrazzo, T. Sohier, I. E. Castelli, A. Cepellotti, G. Pizzi and N. Marzari, *Nat. Nanotechnol.*, 2018, **13**, 246-252.
62. W. Kohn and L. J. Sham, *Physical review*, 1965, **140**, A1133.
63. J. M. Soler, E. Artacho, J. D. Gale, A. García, J. Junquera, P. Ordejón and D. Sánchez-Portal, *Journal of Physics: Condensed Matter*, 2002, **14**, 2745.
64. A. García, N. Papior, A. Akhtar, E. Artacho, V. Blum, E. Bosoni, P. Brandimarte, M. Brandbyge, J. I. Cerdá and F. Corsetti, *The Journal of chemical physics*, 2020, **152**.
65. J. Oroya, A. Martín, M. Callejo, M. García-Mota and F. Marchesin, *SIMUNE Atomistics*, 2014.
66. J. P. Perdew, K. Burke and M. Ernzerhof, *Physical review letters*, 1996, **77**, 3865.
67. M. Dion, H. Rydberg, E. Schröder, D. C. Langreth and B. I. Lundqvist, *Physical review letters*, 2004, **92**, 246401.
68. J. Klimeš, D. R. Bowler and A. Michaelides, *Journal of Physics: Condensed Matter*, 2009, **22**, 022201.
69. W. Tang, E. Sanville and G. Henkelman, *Journal of Physics: Condensed Matter*, 2009, **21**, 084204.
70. H. J. Monkhorst and J. D. Pack, *Physical review B*, 1976, **13**, 5188.
71. C. D. Sherrill, *School of chemistry and biochemistry, Georgia Institute of Technology*, 2010, **130**.
72. S. Slathia, B. Ipaves, C. Campos de Oliveira, S. D. Negedu, S. Sarkar, P. A. Autreto and C. S. Tiwary, *Langmuir*, 2024, **40**, 15731-15740.
73. A. Chakraborty, B. Ipaves, C. Campos de Oliveira, S. D. Negedu, S. Sarkar, B. Lahiri, P. A. Autreto and C. S. Tiwary, *ACS Applied Engineering Materials*, 2024, **2**, 1935-1947.
74. J. Gomez Quispe, B. Ipaves, D. S. Galvao and P. A. d. S. Autreto, *ACS Omega*, 2024, **9**, 39195-39201.
75. G. Wang, S. Zhang, F. A. Umran, X. Cheng, N. Dong, D. Coghlan, Y. Cheng, L. Zhang, W. J. Blau and J. Wang, *Appl. Phys. Lett.*, 2014, **104**.
76. J. Li, Z. Zhang, J. Yi, L. Miao, J. Huang, J. Zhang, Y. He, B. Huang, C. Zhao and Y. Zou, *Nanophotonics*, 2020, **9**, 2415-2424.
77. G. Wang, S. Zhang, X. Zhang, L. Zhang, Y. Cheng, D. Fox, H. Zhang, J. N. Coleman, W. J. Blau and J. Wang, *Photonics Research*, 2015, **3**, A51-A55.
78. J. Wang, Y. Hernandez, M. Lotya, J. N. Coleman and W. J. Blau, *Advanced Materials*, 2009, **21**, 2430-2435.

79. L. Wu, X. Yuan, D. Ma, Y. Zhang, W. Huang, Y. Ge, Y. Song, Y. Xiang, J. Li and H. Zhang, *Small*, 2020, **16**, 2002252.
80. X. Sun, K. Zheng, M. Cai, J. Bao and X. Chen, *Applied Surface Science*, 2019, **491**, 690-697.
81. L. Cheng and Y. Liu, *Journal of the American Chemical Society*, 2018, **140**, 17895-17900.
82. M. Orlita, C. Faugeras, P. Plochocka, P. Neugebauer, G. Martinez, D. K. Maude, A.-L. Barra, M. Sprinkle, C. Berger and W. A. de Heer, *Physical review letters*, 2008, **101**, 267601.
83. G. Long, D. Maryenko, J. Shen, S. Xu, J. Hou, Z. Wu, W. K. Wong, T. Han, J. Lin and Y. Cai, *Nano Letters*, 2016, **16**, 7768-7773.
84. S.-L. Li, K. Tsukagoshi, E. Orgiu and P. Samorì, *Chemical Society Reviews*, 2016, **45**, 118-151.
85. S. Yu, H. D. Xiong, K. Eshun, H. Yuan and Q. Li, *Applied Surface Science*, 2015, **325**, 27-32.
86. A. Allain and A. Kis, *ACS nano*, 2014, **8**, 7180-7185.
87. S. Kumar and U. Schwingenschlogl, *Chemistry of Materials*, 2015, **27**, 1278-1284.
88. D. Ovchinnikov, A. Allain, Y.-S. Huang, D. Dumcenco and A. Kis, *ACS nano*, 2014, **8**, 8174-8181.
89. R. Maiti, M. A. S. R. Saadi, R. Amin, V. O. Ozcelik, B. Uluutku, C. Patil, C. Suer, S. Solares and V. J. Sorger, *ACS Applied Electronic Materials*, 2021, **3**, 3781-3788.
90. F. Dabby, T. Gustafson, J. Whinnery, Y. Kohanzadeh and P. Kelley, *Applied Physics Letters*, 1970, **16**, 362-365.
91. Y. Wang, Y. Tang, P. Cheng, X. Zhou, Z. Zhu, Z. Liu, D. Liu, Z. Wang and J. Bao, *Nanoscale*, 2017, **9**, 3547-3554.
92. S. Goswami, C. C. de Oliveira, B. Ipaves, P. L. Mahapatra, V. Pal, S. Sarkar, P. A. Autreto, S. K. Ray and C. S. Tiwary, *Laser Photonics Rev.*, 2025, 2400999.
93. C. M. Vest and M. Lawson, 1972.
94. R. Karimzadeh, *Journal of optics*, 2012, **14**, 095701.
95. G. Roux, D. Roberts, G. Perron and J. E. Desnoyers, *Journal of Solution Chemistry*, 1980, **9**, 629-647.
96. W. Steele, R. Chirico, A. Nguyen, I. Hossenlopp and N. Smith, *Determination of ideal-gas enthalpies of formation for key compounds*, National Inst. for Petroleum and Energy Research, Bartlesville, OK (United …, 1991.
97. D. Weng, C. Ling, J. He, Q. Cui, C. Xu and B. Gu, Nanoscale, 2026, 18, 3941-3953.
98. S. K. Nayak, M. S. Ahmed, R. Murali, B. Bhavani, S. Prasanthkumar, L. Giribabu and S. S. K. Raavi, Journal of Materials Chemistry C, 2024, 12, 9841-9852.
99. S. Suresh, T. Thomas and S. Thomas, Journal of Non-Crystalline Solids, 2024, 640, 123103.
100. P. Dey, P. Pal, B. K. Das, S. Bhattacharjee, N. Chakraborty, B. Das, S. Ruidas and K. K. Chattopadhyay, Laser & Photonics Reviews, n/a, e02455.
101. P. Dey, N. Chakraborty, M. Samanta, B. Das and K. K. Chattopadhyay, Physical Chemistry Chemical Physics, 2024, 26, 20112-20122.
102. K. V. Jayaprasad, T. Thomas, M. Vaishakh and S. Thomas, Physica E: Low-dimensional Systems and Nanostructures, 2026, 175, 116378.
103. A. Shaw, S. Das, N. Chakraborty, S. Goswami, B. Das and K. K. Chattopadhyay, Optical Materials, 2024, 157, 116191.
104. M. Babu, S. R. Bongu, P. P. Shetty, E. Varrla, G. R. Reddy and J. Bingi, Materials Science in Semiconductor Processing, 2023, 168, 107831.

105. N. Chakraborty, B. Das, A. Roy, P. Dey, B. Das and K. K. Chattopadhyay, ACS Applied Optical Materials, 2024, 2, 1454-1465.